Supporting Information for "Seismic Evidence for Craton Formation by Underplating and Development of the MLD"

Alistair Boyce[1], Thomas Bodin[1], Stéphanie Durand[1], Dorian Soergel[1,2], Eric Debayle[1]

[1]Université Claude Bernard Lyon 1, ENS de Lyon, CNRS, UMR 5276 LGL-TPE, F-69622, Villeurbanne, France

[2]Department of Earth and Planetary Science, University of California, Berkeley, CA 94720, USA

Corresponding author: Alistair Boyce, alistair.boyce@univ-lyon1.fr

Contents of this file

Introduction

This supplement provides background information on published global shear wave velocity and radial anisotropy models, further methodological details, testing and results. The data files, inversion software package and outputs as well as plotting codes are available under the doi: 10.5281/zenodo.8167649 (Boyce, 2023).

Models of Global Shear Velocity and Radial Anisotropy

Figures S1–S3 show 12 radially anisotropic global tomographic models plotted at 150 km depth with respect to the mean value in each model (Figure S1), anisotropic PREM (Figure S2) and the absolute value (Figure S3). Figures S4–S5 show V_{SV} and ξ profiles extracted at 12 cratonic locations from global tomographic models to 660 km depth.

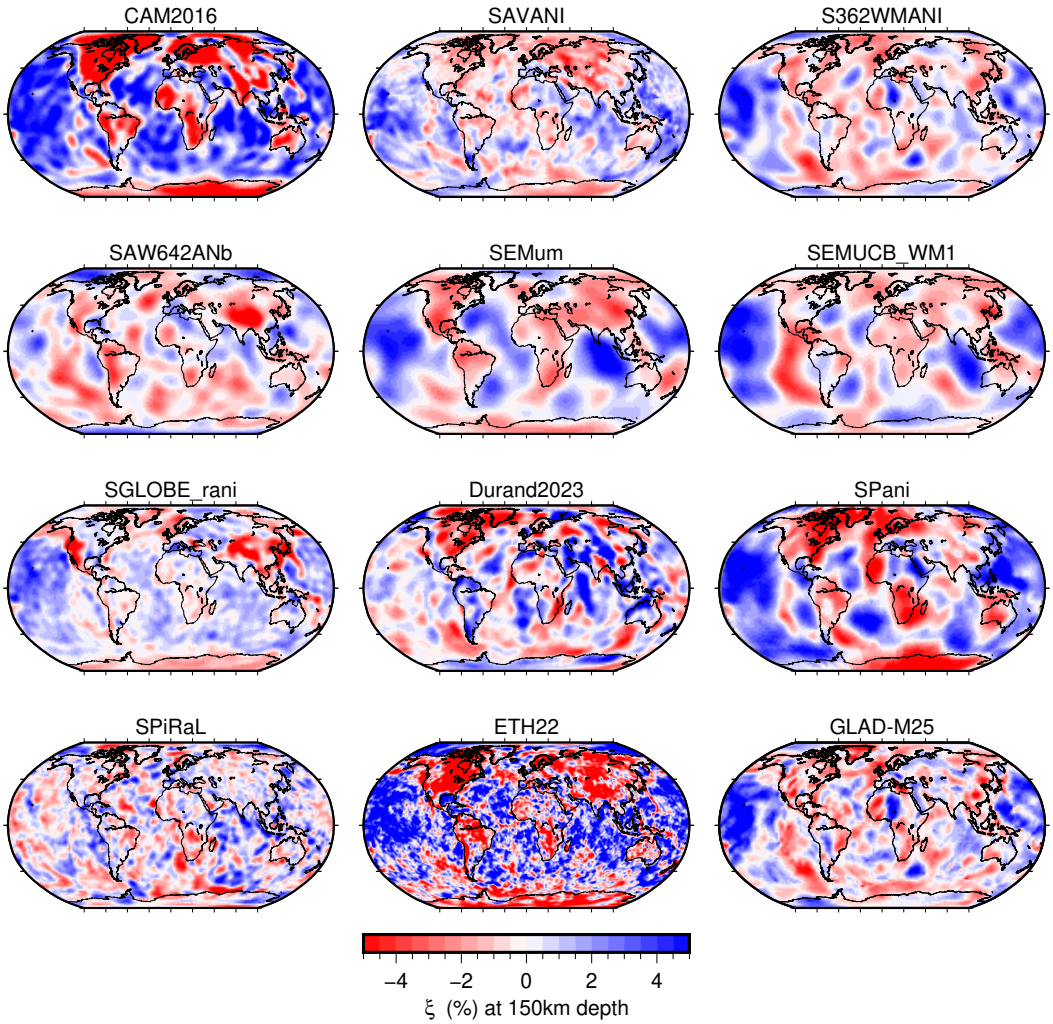

Figure S1. Twelve global radially anisotropic tomographic models plotted at 150 km depth with respect to the mean value in each model. Plotted models: CAM2016 (Priestley et al., 2020), SAVANI (Auer et al., 2014), S362WMANI (Kustowski et al., 2008), SAW642ANb (Panning et al., 2010), SEMum (Lekić & Romanowicz, 2011), SEMUCB_WM1 (French & Romanowicz, 2014), SGLOBErani (Chang et al., 2015), *Durand2023 - unpublished*, SPani (Tesoniero et al., 2015), SPiRaL (Simmons et al., 2021), ETH22 (Thrastarson et al., 2022), GLAD-M25 (Lei et al., 2020).

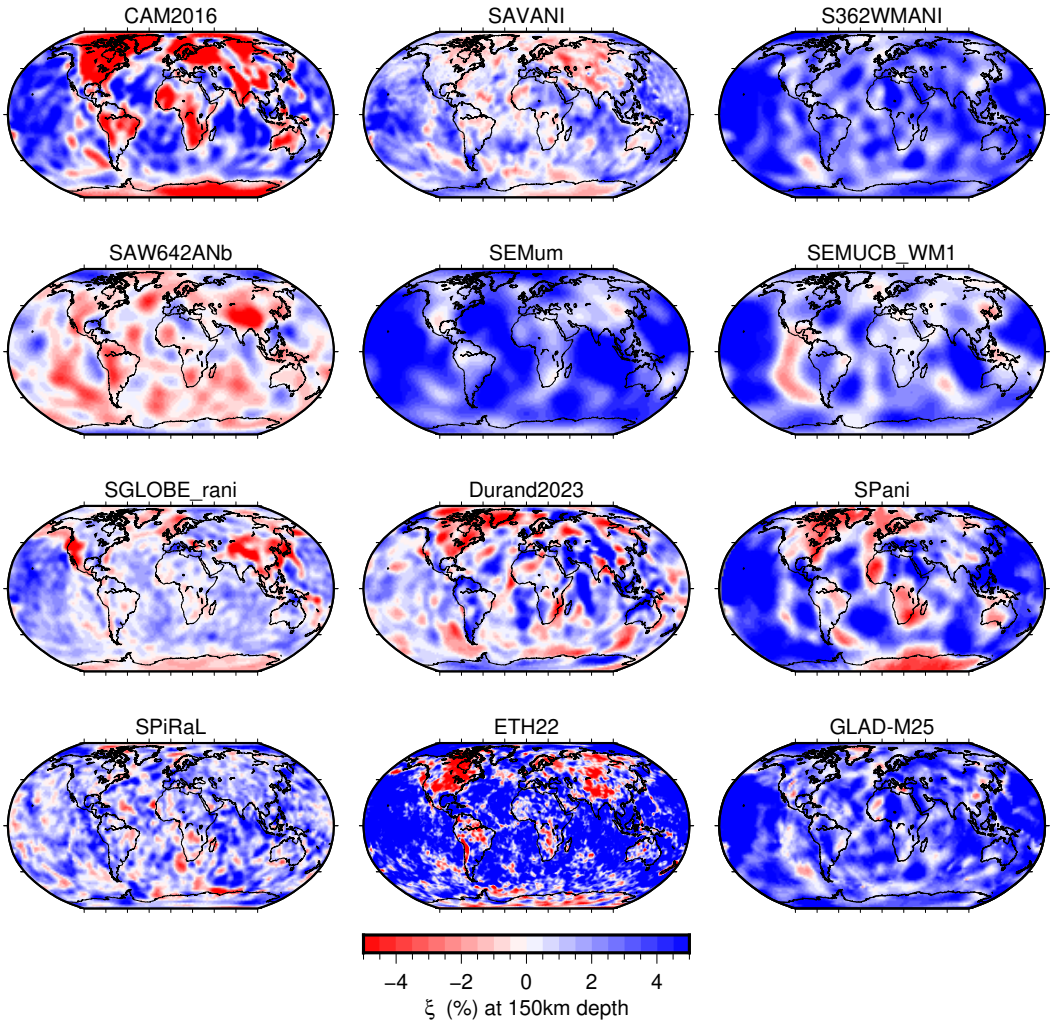

Figure S2. Twelve global radially anisotropic tomographic models plotted at 150 km depth with respect to anisotropic PREM model (Dziewonski & Anderson, 1981). Plotted models: CAM2016 (Priestley et al., 2020), SAVANI (Auer et al., 2014), S362WMANI (Kustowski et al., 2008), SAW642ANb (Panning et al., 2010), SEMum (Lekić & Romanowicz, 2011), SEMUCB_WM1 (French & Romanowicz, 2014), SGLOBErani (Chang et al., 2015), *Durand2023 - unpublished*, SPani (Tesoniero et al., 2015), SPiRaL (Simmons et al., 2021), ETH22 (Thrastarson et al., 2022), GLAD-M25 (Lei et al., 2020).

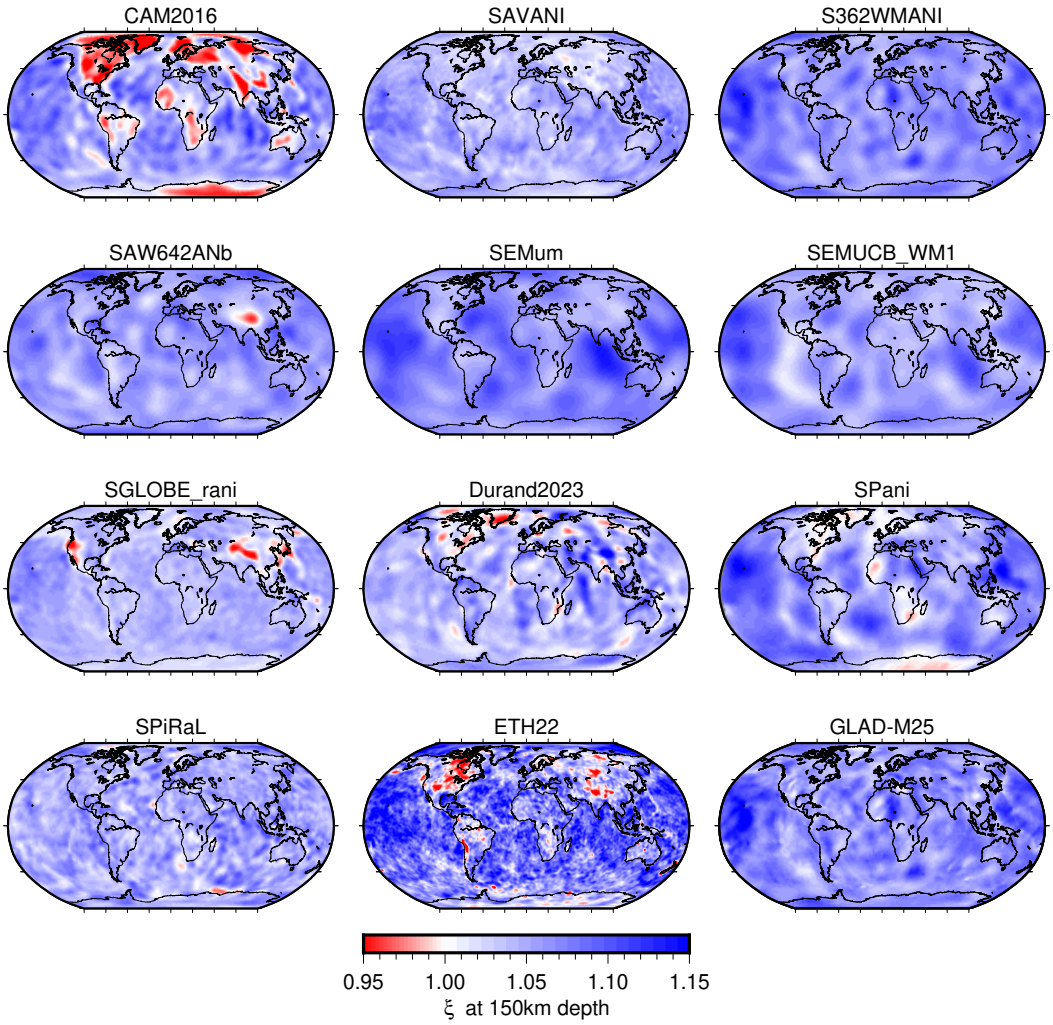

Figure S3. Twelve global radially anisotropic tomographic models plotted as the absolute value at 150 km depth. Note asymmetric color scale. Plotted models: CAM2016 (Priestley et al., 2020), SAVANI (Auer et al., 2014), S362WMANI (Kustowski et al., 2008), SAW642ANb (Panning et al., 2010), SEMum (Lekić & Romanowicz, 2011), SEMUCB_WM1 (French & Romanowicz, 2014), SGLOBErani (Chang et al., 2015), *Durand2023 - unpublished*, SPani (Tesoniero et al., 2015), SPiRaL (Simmons et al., 2021), ETH22 (Thrastarson et al., 2022), GLAD-M25 (Lei et al., 2020).

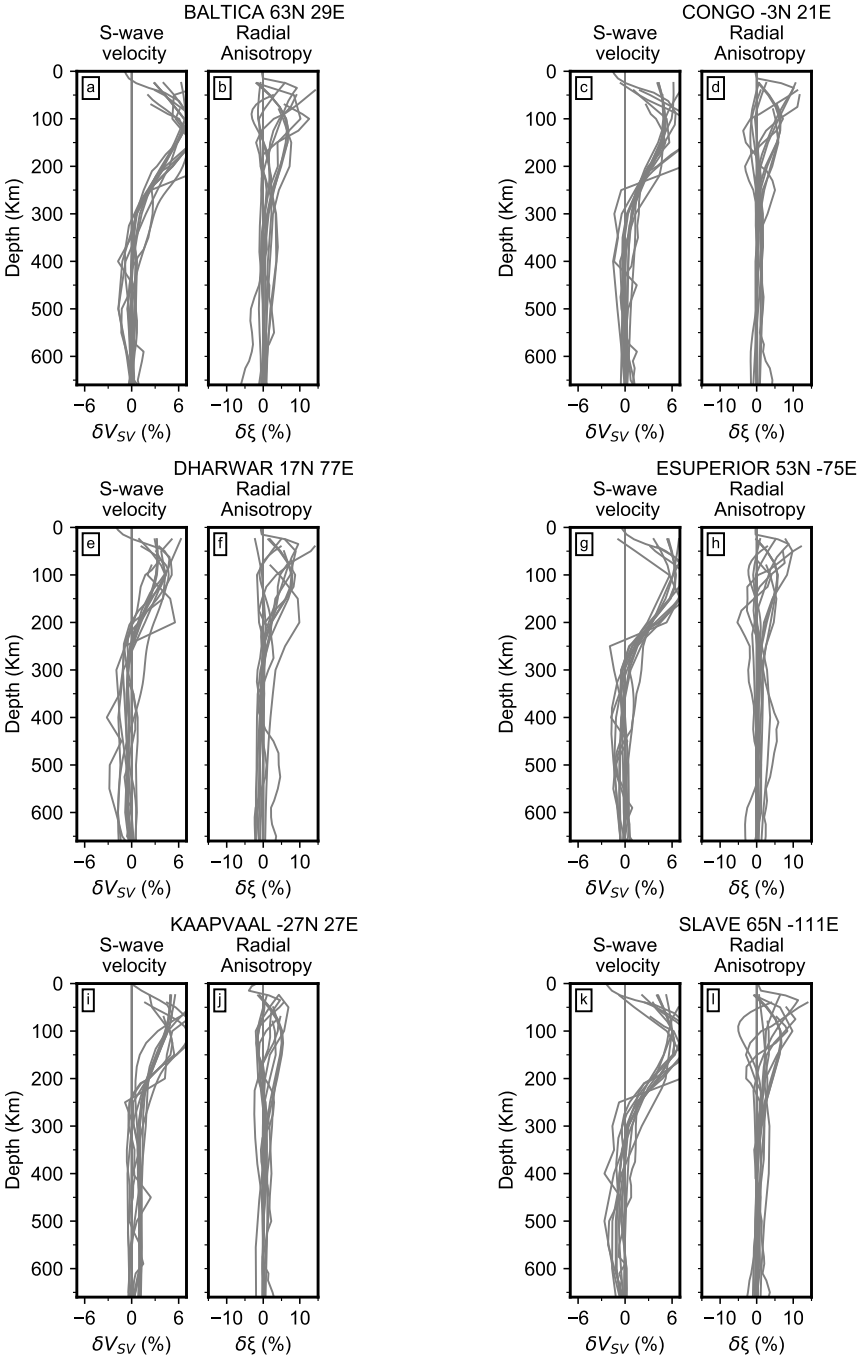

Figure S4. V_{SV} and ξ profiles extracted from global tomographic models to 660 km depth at 6 cratonic locations: Baltica, Congo, Dharwar, East Superior, Kaapvaal, Slave. V_{SV} profiles plotted with respect to PREM (Dziewonski & Anderson, 1981) or STW105 (Kustowski et al., 2008). ξ plotted as deviation from isotropy. Tomographic models: *Durand2023 - unpublished*, CAM2016 (Priestley et al., 2020), SEMum (Lekić & Romanowicz, 2011), SAVANI (Auer et al., 2014), S362WMANI (Kustowski et al., 2008), S362ANI (Kustowski et al., 2008), S362ANI_M (Moulik & Ekström, 2014), SAW642AN (Megnin & Romanowicz, 2000), SAW642ANb (Panning et al., 2010), SEMUCB_WM1 (French & Romanowicz, 2014), SGLOBErani (Chang et al., 2015), SPani (Tesoniero et al., 2015).

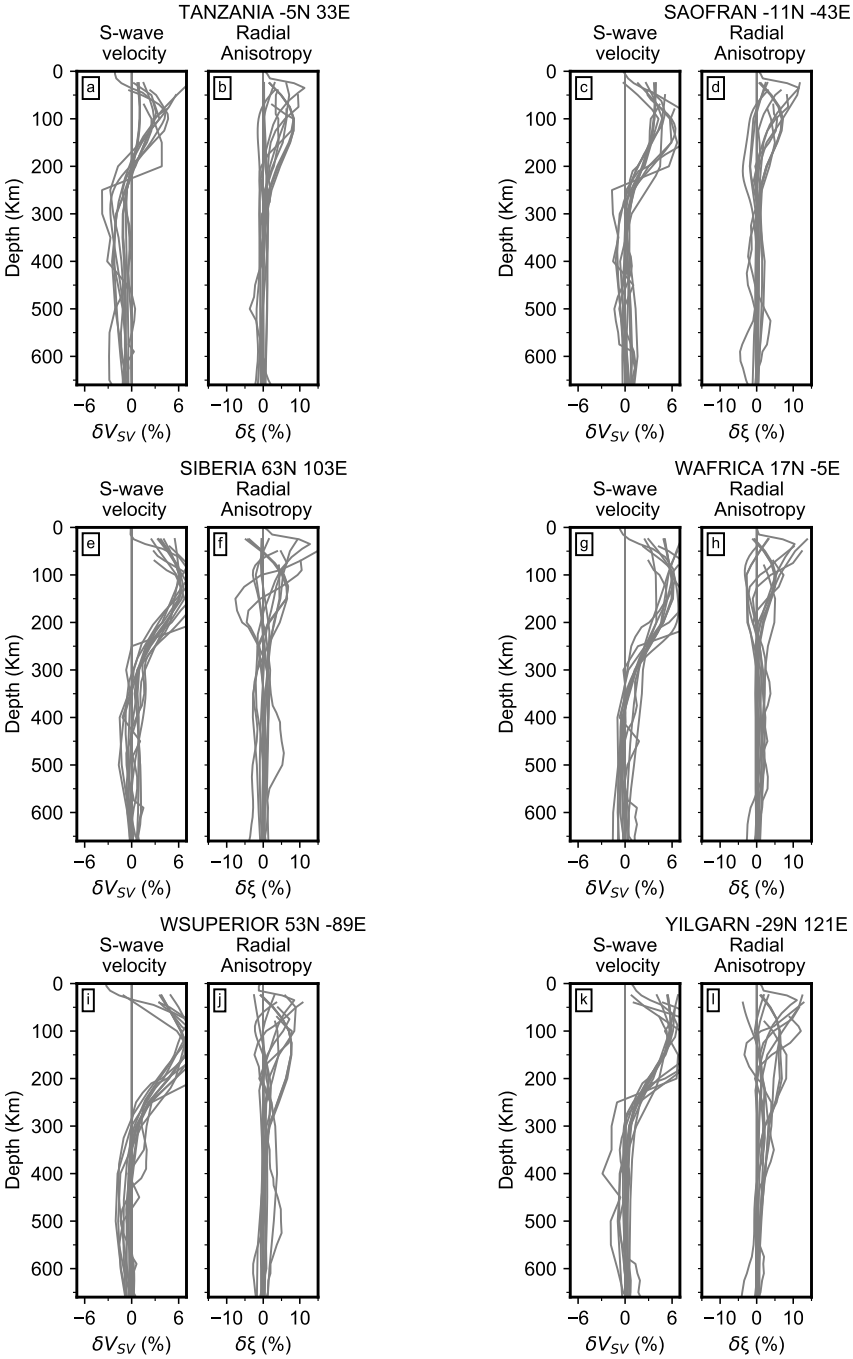

Figure S5. V_{SV} and ξ profiles extracted from global tomographic models to 660 km depth at 6 cratonic locations: Tanzania, Sao Francisco, Siberia, West Africa, West Superior, Yilgarn. V_{SV} profiles plotted with respect to PREM (Dziewonski & Anderson, 1981) or STW105 (Kustowski et al., 2008). ξ plotted as deviation from isotropy. Tomographic models: *Durand2023 - unpublished*, CAM2016 (Priestley et al., 2020), SEMum (Lekić & Romanowicz, 2011), SAVANI (Auer et al., 2014), S362WMANI (Kustowski et al., 2008), S362ANI (Kustowski et al., 2008), S362ANI_M (Moulik & Ekström, 2014), SAW642AN (Megnin & Romanowicz, 2000), SAW642ANb (Panning et al., 2010), SEMUCB_WM1 (French & Romanowicz, 2014), SGLOBErani (Chang et al., 2015), SPani (Tesoniero et al., 2015).

Dispersion Curve Data

Figures S6–S8 detail dispersion curve data extracted from phase velocity maps of Durand et al. (2015) and Ho et al. (2016) for 12 cratonic locations (Figure S6), 5 tectonically active locations (Figure S7) and six cross section points across North America (Figure S8).

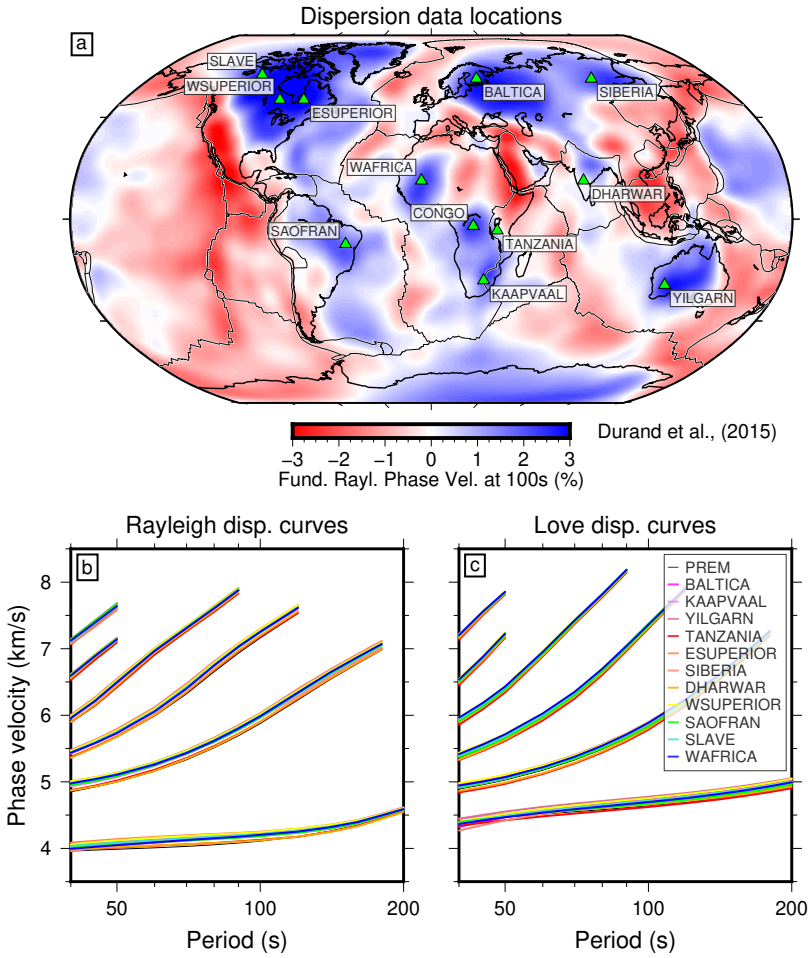

Figure S6. (a) Fundamental mode Rayleigh wave phase velocity map at 100 s period from Durand et al. (2015) with twelve cratonic locations shown (green triangles) inverted in Figures S16–S21. Rayleigh (b) and Love (c) fundamental and overtone (1–5) dispersion curves used in the inversions.

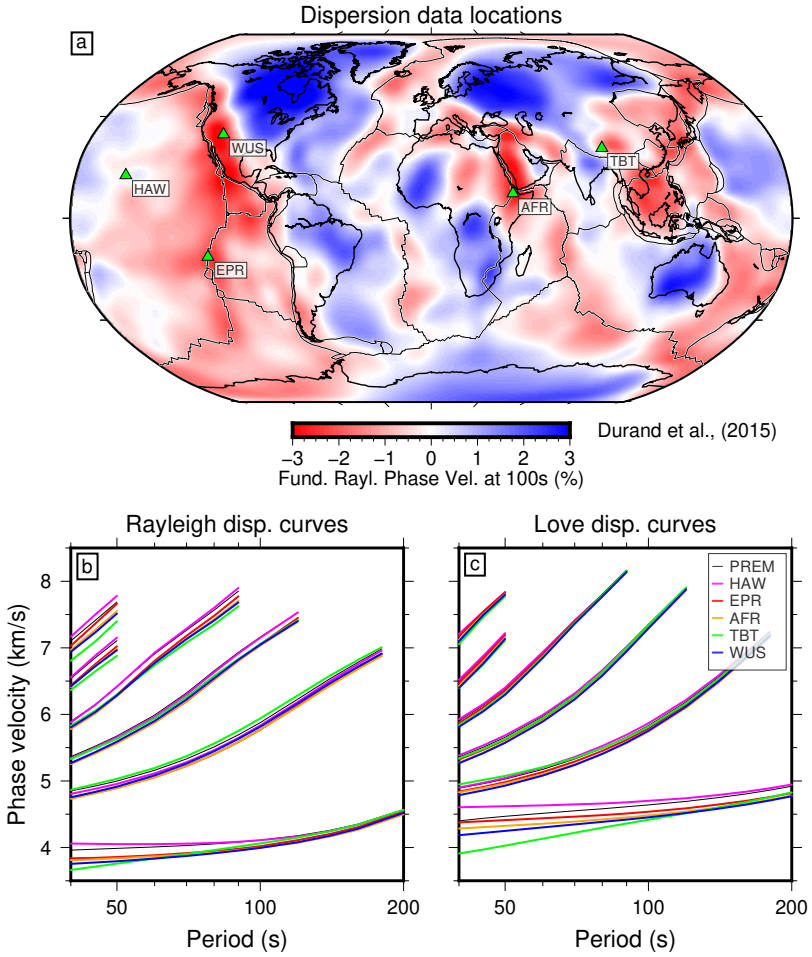

Figure S7. (a) Fundamental mode Rayleigh wave phase velocity map at 100 s period from Durand et al. (2015) with five active tectonic locations shown (green triangles) inverted in Figures S18–S22. Rayleigh (b) and Love (c) fundamental and overtone (1–5) dispersion curves used in the inversions. AFR: Afar Depression, EPR: East Pacific Rise, HAW: Hawaii, TBT: Tibet, WUS: Western US.

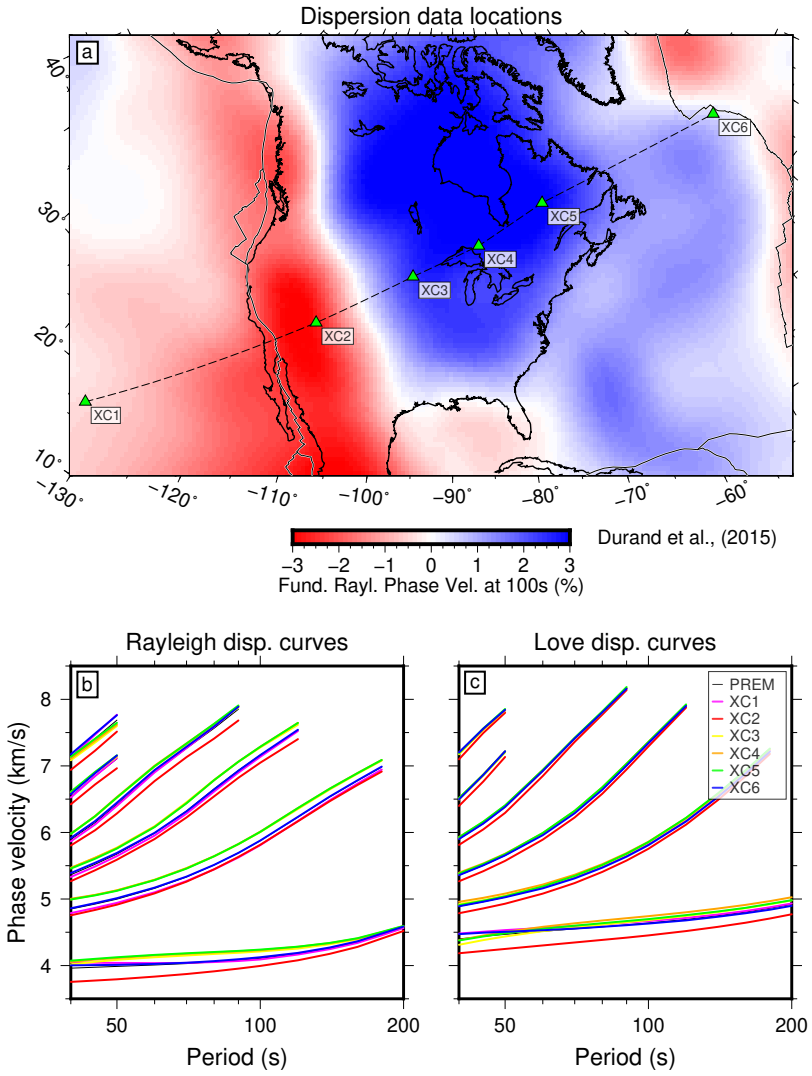

Figure S8. (a) Fundamental mode Rayleigh wave phase velocity map at 100 s period from Durand et al. (2015) with six cross section points across North America shown (green triangles) inverted in Figures S19–S23. Rayleigh (b) and Love (c) fundamental and overtone (1–5) dispersion curves used in the inversions.

Center of the Prior Distribution

To produce the PREM-like model that defines the center of the prior distribution for each Bayesian inversion, we simplify the PREM model (Dziewonski & Anderson, 1981) and merge that with an overlying crust from CRUST1.0 (Laske et al., 2013). First, we shift the mantle transition zone discontinuities to 410 km and 660 km depth. We then remove the 220 km depth discontinuity by linearly interpolating between 220 km and 410 km depth. The model is then decimated between remaining interfaces to speed up forward modeling in Mineos (Masters et al., 2011) and all P- and S-wave radial anisotropy is removed. For each inversion location, we then take the crustal model from CRUST1.0 (Laske et al., 2013) including sedimentary and crystalline rock layers down to the Moho and then smoothly interpolate between this and the next deepest value in the modified PREM model.

Further Methodological Details

Although not an inverted parameter, we test the importance of the P-wave radial anisotropy parameter *Phi* (Φ=V_{PV}/V_{PH}). For cratons we find that data fit is best using ϕ=1, whilst for all inversions across active/young tectonic domains, data fit is best using the following scaling relationship with the inverted parameter ξ (see Montagner & Anderson, 1989):

$$\phi = 1.8 - 0.8\xi$$

Consequently, when using the Bayesian algorithm, all results presented for cratons use ϕ=1, while other locations use the scaling relationship above.

Figure S9 plots the sensitivity of Rayleigh and Love dispersion curve data to parameters V_{SV}, V_{PH} and V_{SH} for selected periods for the fundamental mode and 3rd overtone.

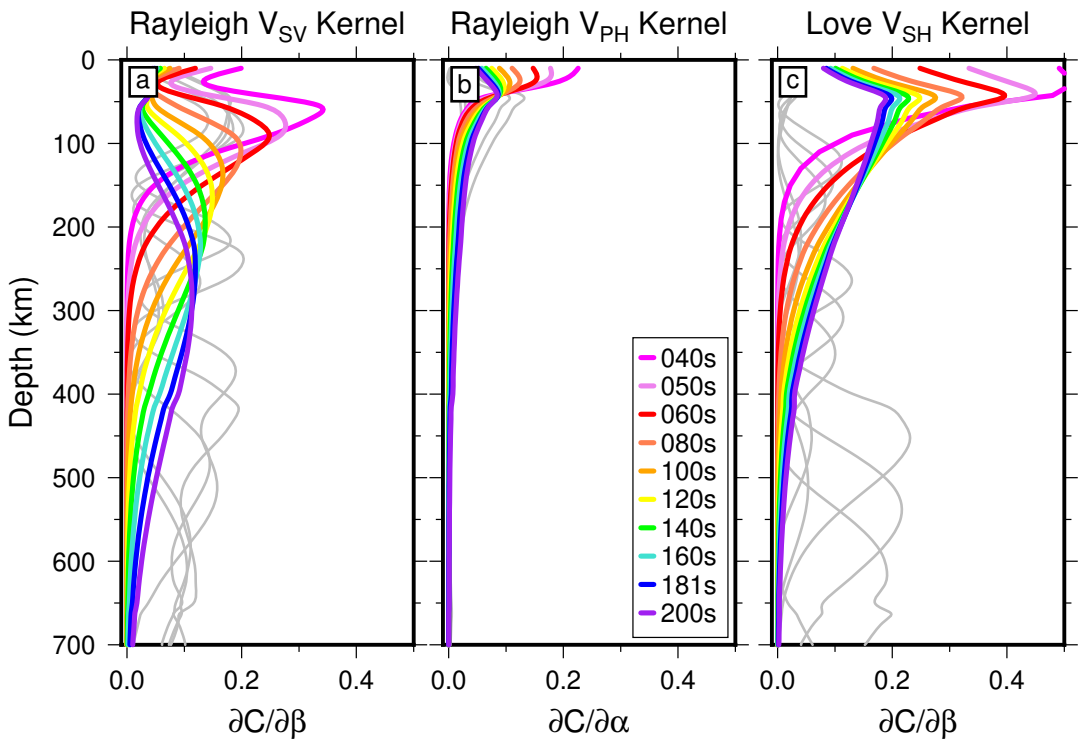

Figure S9. Fundamental mode (colored) and 3rd overtone (gray) phase velocity (C) sensitivity kernels for Rayleigh (V_{SV} and V_{PH}, a,b) and Love (V_{SH}, c) waves at a range of periods for the modified PREM reference model.

Synthetic and Parameterization Tests

Figures S10–S12 show Bayesian and LSQR inversion results of synthetic surface wave dispersion curves (with the same distribution as observed data) from test input models. Synthetic tests are conducted by adding 0.0025 s Gaussian noise to the forward modeled dispersion data from Masters et al. (2011). Compared to real data, we use half the number of samples in the posterior. Inversions are run on 140 independent chains, but still with a burn-in of 300,000 iterations, sampling one in every 50 from the remaining 300,000 iterations to form the posterior distributions.

The Bayesian scheme recovers the input V_{SV} anomalies and ξ anomalies well and importantly, the median model recovers $\delta\xi$=0 (i.e. ξ=1) where there is an absence of radial anisotropy in the input model (Figure S10). It also reliably recovers the vertical extent of V_{SV} and ξ anomalies (Figure S11), with a mean depth uncertainty of 18 km and 9 km, respectively. These estimates are used as uncertainties on transition depths in Figure 2. We note that a presence or lack of positive V_{SV} and ξ anomalies in the shallow mantle and crust (<50 km depth) appears resolved (Figures S10–S11). However, while LSQR inversions (S12) show reasonable recovery of V_{SV} anomalies at upper mantle depths, 'recovered' ξ artifacts are common where $\delta\xi$=0 in the input model where V_{PH}-Fixed parameterizations are used, especially for independent inversion of V_{SV} and V_{SH}.

To verify that crustal heterogeneity does not cause artifacts in our inversion we conduct similar tests to those in Figure S10 but perturb velocity and anisotropy anomalies above the Moho. Figure S13 shows that neither velocity or radial anisotropy anomalies in the crust influence the inversion result in the mantle, in either case where the underlying mantle is anomalous (a–c) or is close to the reference model (d–f).

The flexibility of the Bayesian approach allows us to test the influence of parameterization choices on the posterior distribution. Figure S14 shows the result of inverting real data from the Baltica craton using a parameterization that proposes anisotropic layers directly during the birth of a new layer, rather than an isotropic layer. The value of proposed anisotropy is a small random perturbation around the value from the closest existing layer. The value of ξ in all layers can therefore approximate, but may not equal unity exactly. ξ anomalies show much greater variability below 150 km depth compared to the case where we also allow isotropic layers. Furthermore additional ξ artifacts may be present in the shallow crust and deepest portion of the model space (Figure S14).

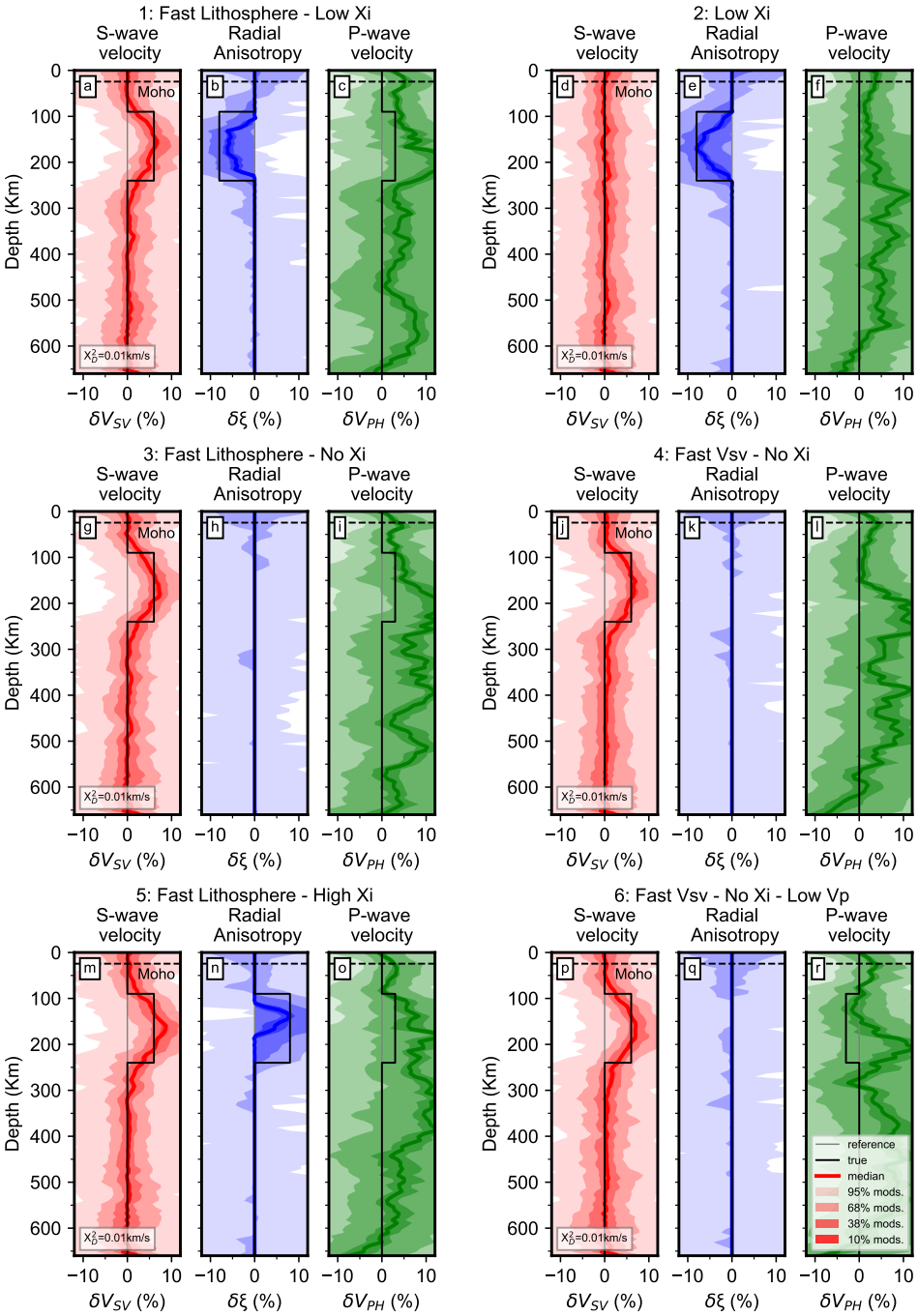

Figure S10. Posterior distributions for V_{SV} (a,d,g,j,m,p), ξ (b,e,h,k,n,q) and V_{PH} (c,f,i,l,o,r) for six synthetic tests with respect to the isotropic reference model (gray line). The preferred median model for V_{SV} (red), ξ (blue) and V_{PH} (green) is shown as a solid, bold line. Confidence intervals (percentage of models) are shown as varying shades of red (V_{SV}), blue (ξ) and green (V_{PH}). The true model (thick black line) and data misfit (X_D^2) are also shown.

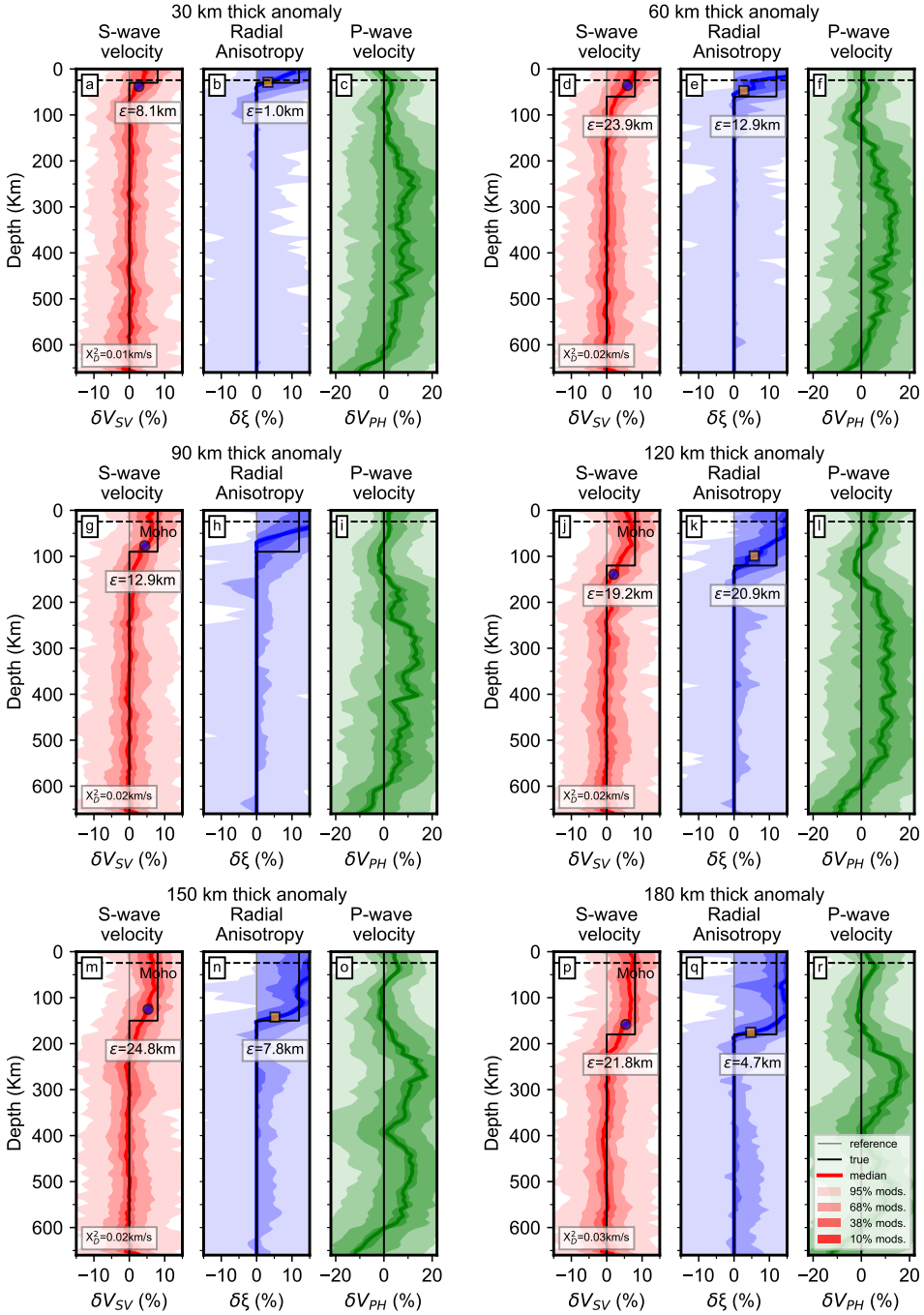

Figure S11. Posterior distributions for V_{SV} (a,d,g,j,m,p), ξ (b,e,h,k,n,q) and V_{PH} (c,f,i,l,o,r) with respect to the isotropic reference model (gray line) for six synthetic test models containing a positive anomaly for both V_{SV} and ξ with increasing vertical extent from 30–180 km depth. The preferred median model for V_{SV} (red), ξ (blue) and V_{PH} (green) is shown as a solid, bold line. Confidence intervals (percentage of models) are shown as varying shades of red (V_{SV}), blue (ξ) and green (V_{PH}). The true model (thick black line) and data misfit (X_D^2) are also shown. Blue circles and orange squares plot depth of maximum negative gradient (transition depth) within ±25 km depth of the base of the synthetic anomaly within the V_{SV} and ξ posterior distributions (where possible). ε: depth difference between transition depths and known interface in synthetic model.

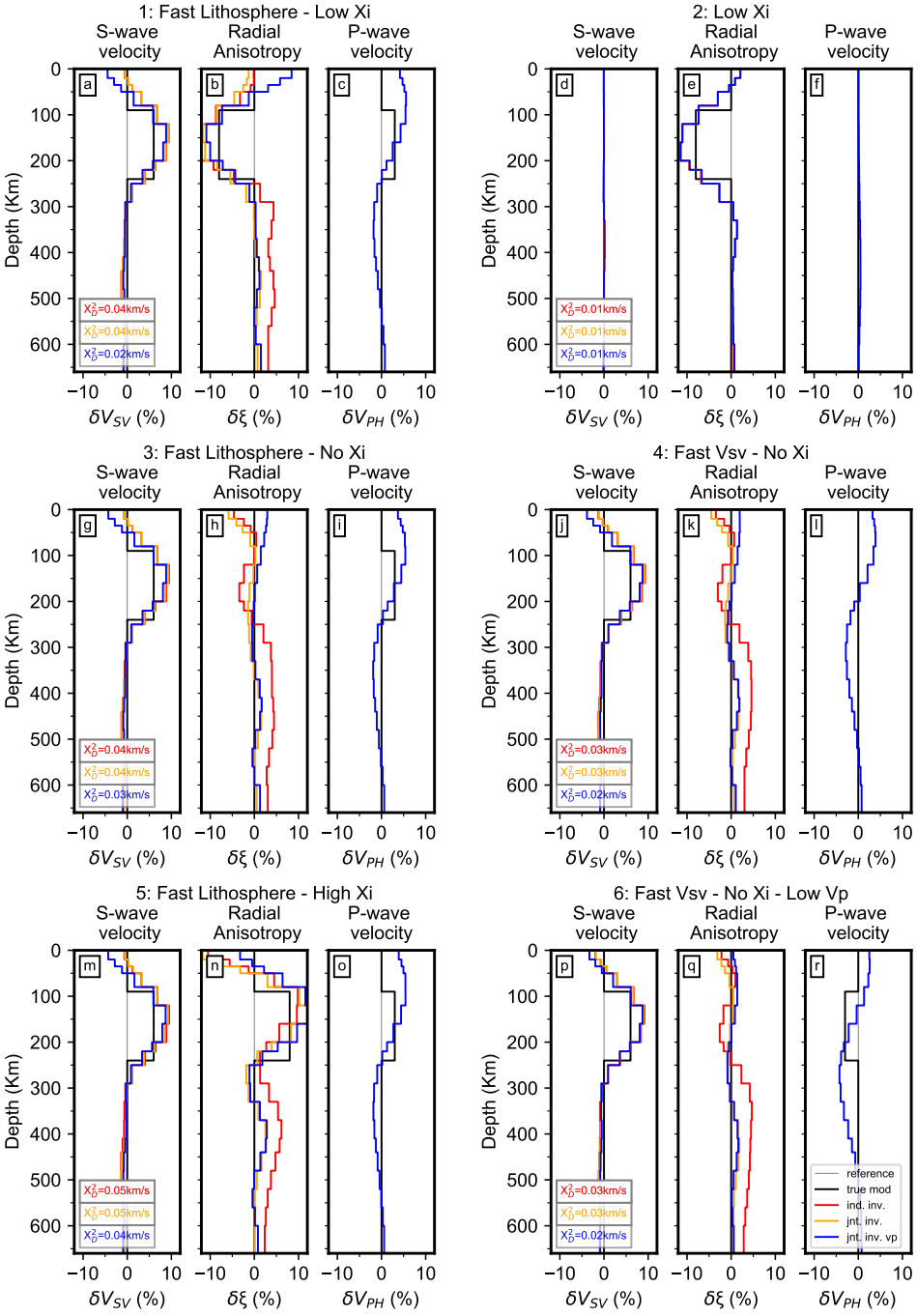

Figure S12. Six synthetic models inverted using variably parameterized LSQR algorithm after Tarantola and Valette (1982); Durand et al. (2015). V_{SV} (a,d,g,j,m,p), ξ (b,e,h,k,n,q) and V_{PH} (c,f,i,l,o,r) shown in percent deviation from the isotropic reference model. Red curve: Independent inversion for V_{SV} and V_{SH}, Orange curve: Joint inversion for V_{SV} and V_{SH}, Blue curve: Joint inversion for V_{SV}, V_{SH} and V_{PH}. The blue curve overlies red and orange curves in cases where inversion outputs are identical. Chi squared data (X_D^2) fits shown. Reference model (gray line), True model (thick black line).

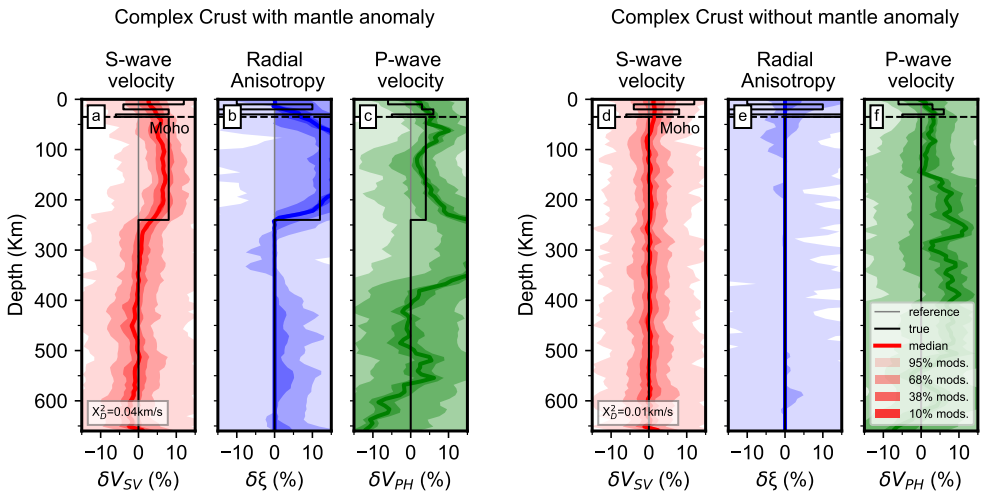

Figure S13. Posterior distributions for V_{SV} (a,d), ξ (b,e) and V_{PH} (c,f) for complex crust synthetic tests with (Left hand side) and without (Right hand side) an underlying mantle anomaly, plotted with respect to the isotropic reference model (gray line). The preferred median model for V_{SV} (red), ξ (blue) and V_{PH} (green) is shown as a solid, bold line. Confidence intervals (percentage of models) are shown as varying shades of red (V_{SV}), blue (ξ) and green (V_{PH}). The true model (thick black line) and data misfit (X_D^2) are also shown.

Figure S15 shows that when V_{PH} in all layers is fixed to the reference model, the model fit (X_M^2) is worse as well as the mean depth difference between transition depths and known interfaces in synthetic test models (14.3 km, d–f) compared to the V_{PH}-Free parameterization (10.0 km, a–c). As expected, the fit to the data is also worse in the V_{PH}-Fixed parameterization compared to the V_{PH}-Free parameterization for both synthetic and real data examples. Furthermore, within the real data example, distinct negative radial anisotropy is produced in the crust and a low velocity zone within the lithosphere is not revealed when using a V_{PH}-Fixed parameterization (Figure S15g–l). This trend is also clear in radial anisotropy results for synthetic tests using LSQR inversions (Figure S12) where V_{PH}-Fixed parameterizations appear to bias ξ results too.

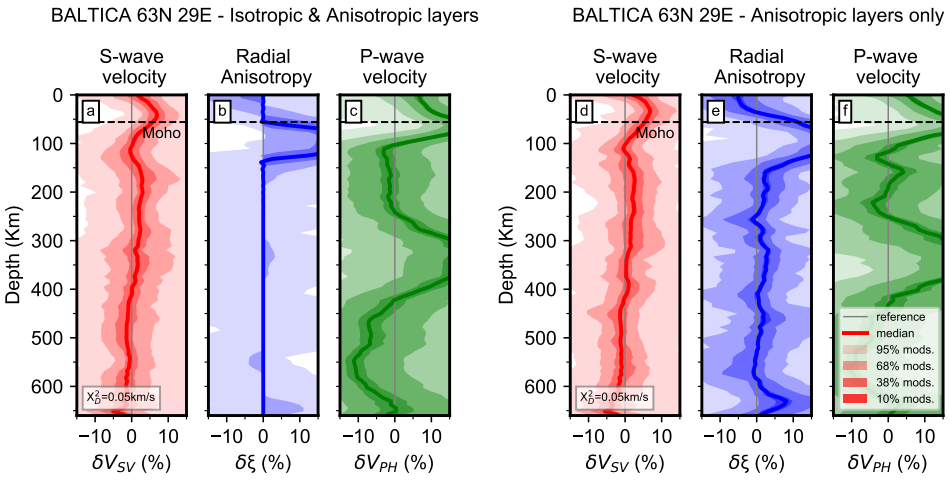

Figure S14. Posterior distributions for V_{SV} (a,d), ξ (b,e) and V_{PH} (c,f) for Bayesian parameterization in which layers can be both isotropic or anisotropic (Left hand side) or all layers are forced to be anisotropic (Right hand side). Models plotted with respect to the isotropic reference model (gray line). The preferred median model for V_{SV} (red), ξ (blue) and V_{PH} (green) is shown as a solid, bold line. Confidence intervals (percentage of models) are shown as varying shades of red (V_{SV}), blue (ξ) and green (V_{PH}). Data misfit (X_D^2) is also reported.

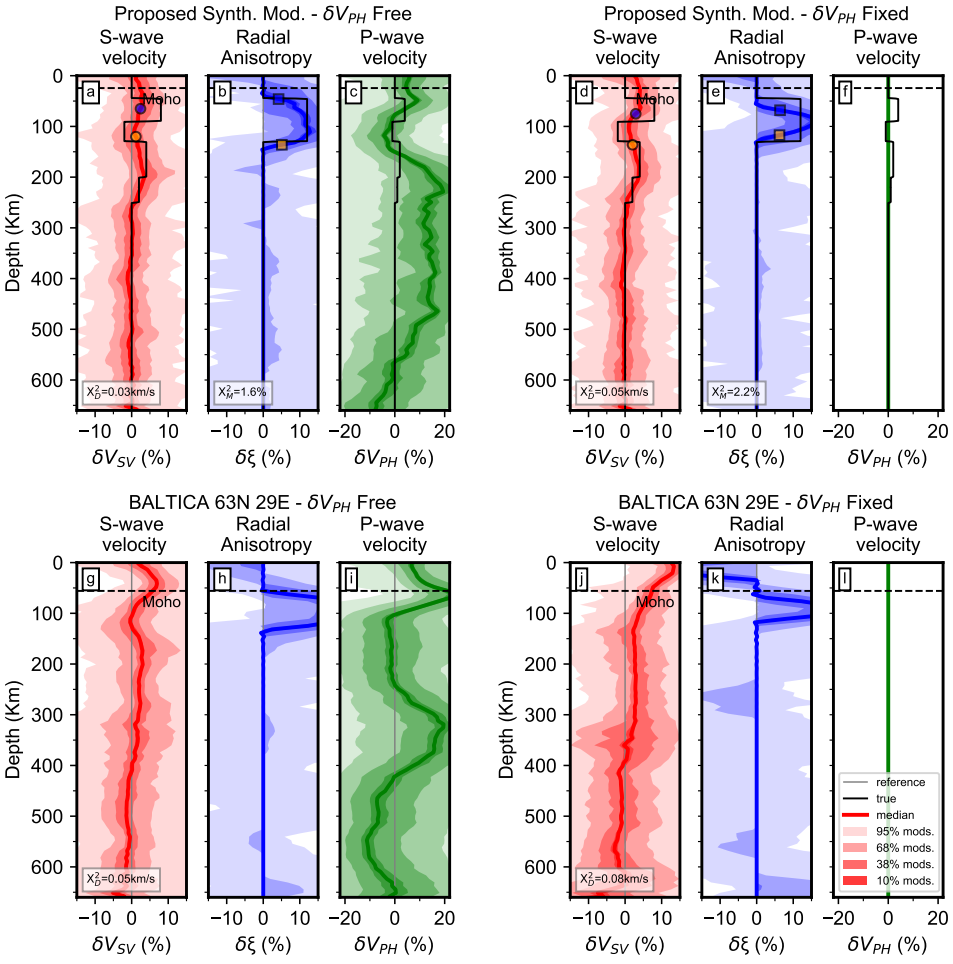

Figure S15. Posterior distributions for V_{SV} (a,d,g,j), ξ (b,e,h,k) and V_{PH} (c,f,i,l) for synthetic model (thick black line, a–f) and real data inversions (g–l). Left hand side shows inversion with V_{PH}-Free parameterization, while the right hand side shows inversion with a V_{PH}-Fixed (to reference model) parameterization. All parameters are plotted with respect to the isotropic reference model (gray line). The preferred median model for V_{SV} (red), ξ (blue) and V_{PH} (green) is shown as a solid, bold line. Confidence intervals (percentage of models) are shown as varying shades of red (V_{SV}), blue (ξ) and green (V_{PH}). Data misfit (X_D^2) is also reported as well as model fit (X_M^2) for synthetic tests (a–f). Blue circles and orange squares plot depth of minimum/maximum gradients (transition depths) within ±25 km depth of the top and base of low velocity zone (V_{SV}) and positive ξ anomaly within the posterior distributions for synthetic tests (a–f).

Bayesian Data Inversions

Figures S16–S19 detail inversion results for twelve craton locations (Figures S16–S17), five tectonically active locations (Figure S18) and six cross section points across North America (Figure S19) computed using the Bayesian algorithm.

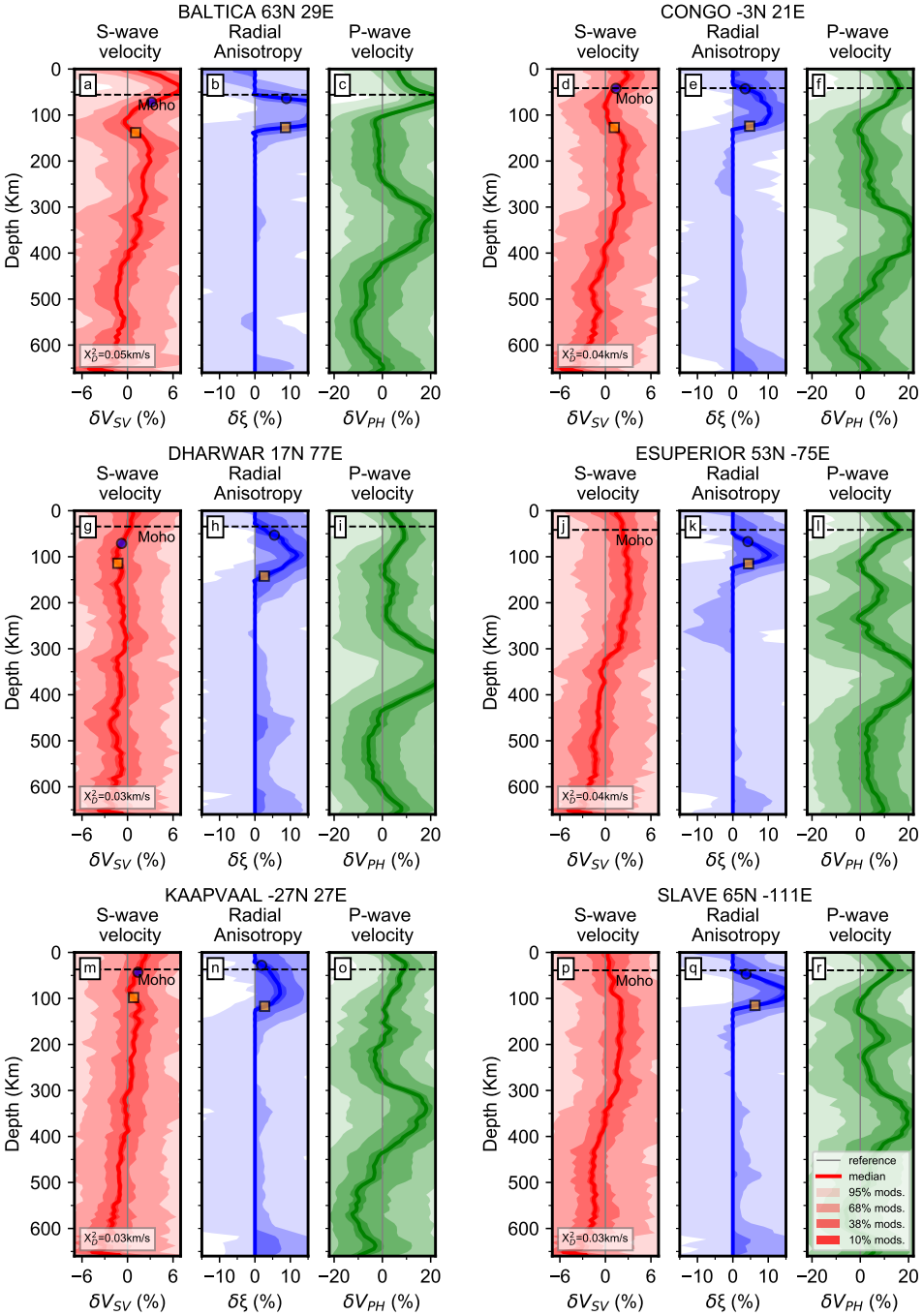

Figure S16. Posterior distributions for V_{SV} (a,d,g,j,m,p), ξ (b,e,h,k,n,q) and V_{PH} (c,f,i,l,o,r) for six cratonic locations (Figure S6) with respect to the isotropic reference model smoothed into Crust1.0 (gray line). The preferred median model for V_{SV} (red), ξ (blue) and V_{PH} (green) is shown as a solid, bold line. Confidence intervals (percentage of models) are shown as varying shades of red (V_{SV}), blue (ξ) and green (V_{PH}). Transition depths (blue circles, orange squares) used in Figure 2 also shown where appropriate. Data misfit (X_D^2) is also reported.

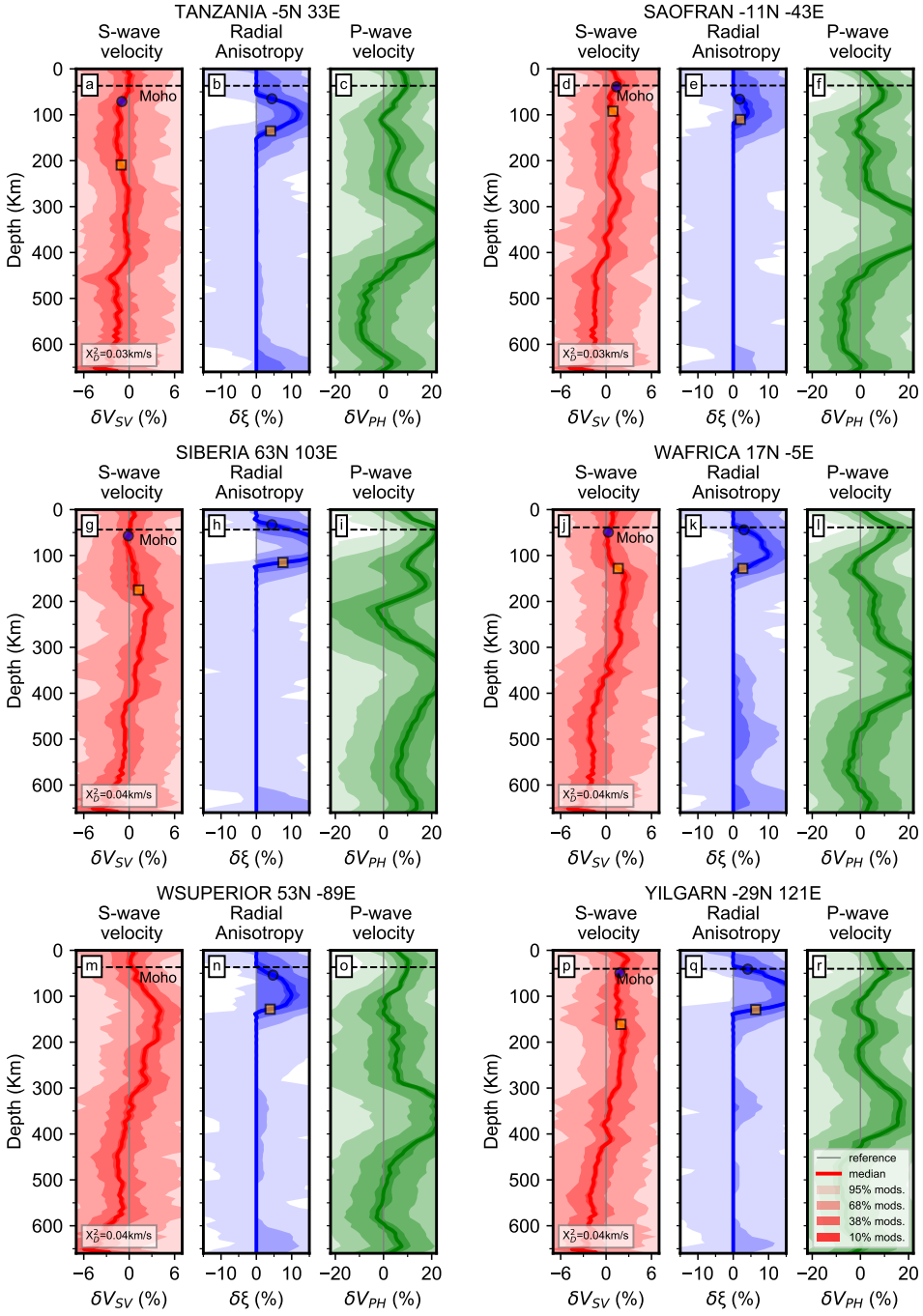

Figure S17. Posterior distributions for V_{SV} (a,d,g,j,m,p), ξ (b,e,h,k,n,q) and V_{PH} (c,f,i,l,o,r) for six cratonic locations (Figure S6) with respect to the isotropic reference model smoothed into Crust1.0 (gray line). The preferred median model for V_{SV} (red), ξ (blue) and V_{PH} (green) is shown as a solid, bold line. Confidence intervals (percentage of models) are shown as varying shades of red (V_{SV}), blue (ξ) and green (V_{PH}). Transition depths (blue circles, orange squares) used in Figure 2 also shown where appropriate. Data misfit (X_D^2) is also reported.

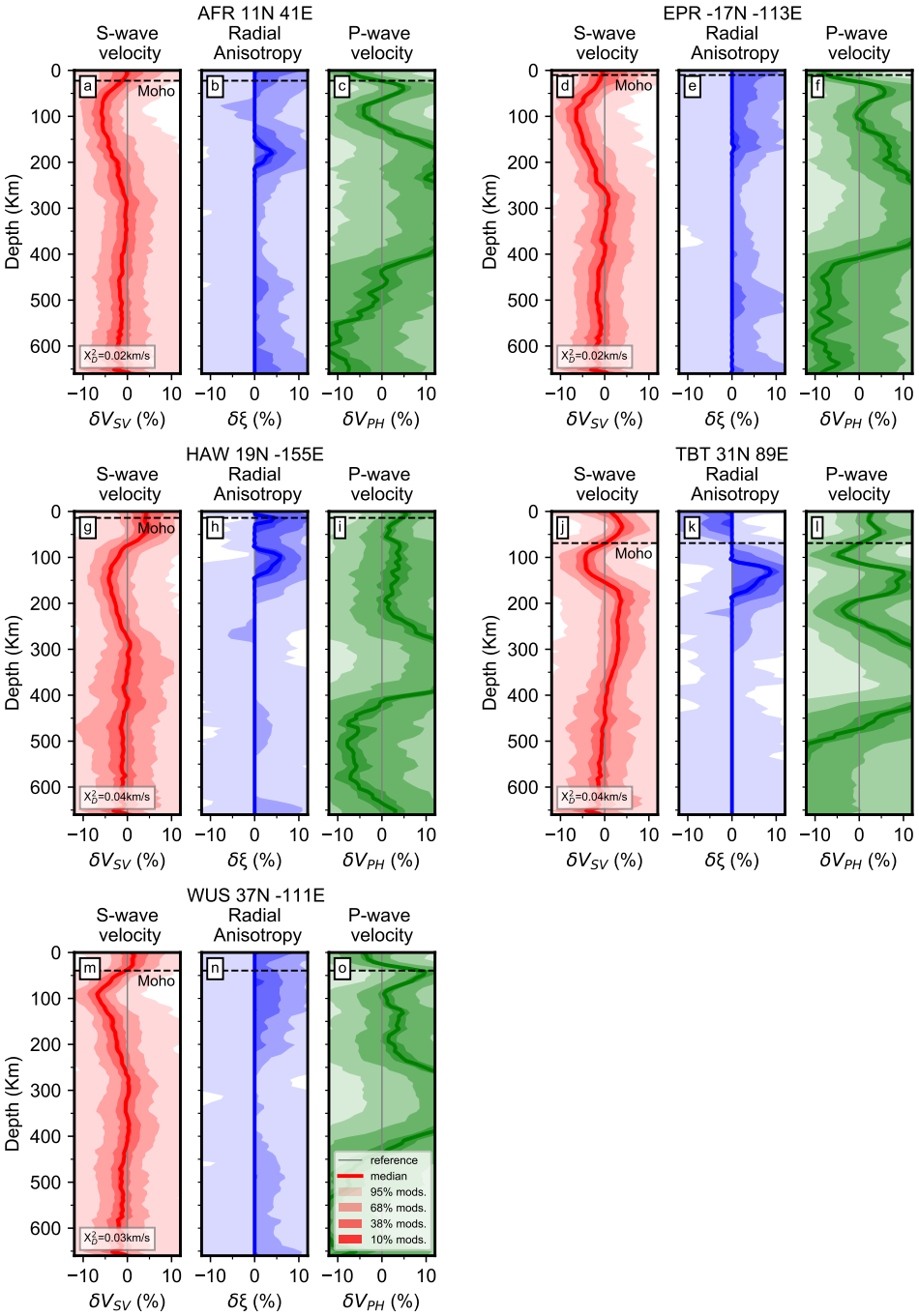

Figure S18. Posterior distributions for V_{SV} (a,d,g,j,m,p), ξ (b,e,h,k,n,q) and V_{PH} (c,f,i,l,o,r) for five active tectonic locations (Figure S7) with respect to an isotropic reference model smoothed into Crust1.0 (gray line). The preferred median model for V_{SV} (red), ξ (blue) and V_{PH} (green) is shown as a solid, bold line. Confidence intervals (percentage of models) are shown as varying shades of red (V_{SV}), blue (ξ) and green (V_{PH}). Data misfit (X^2_D) is also reported.

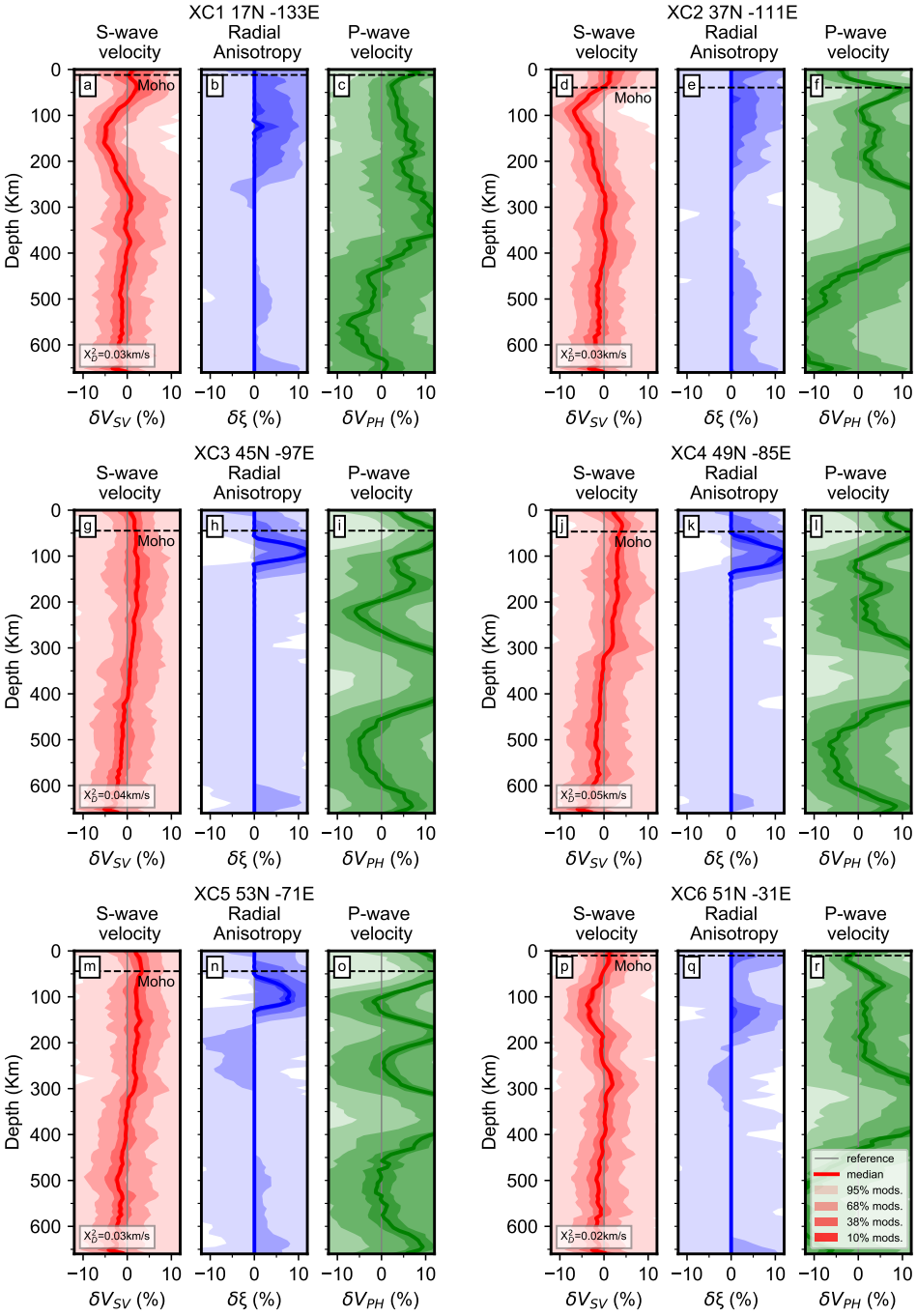

Figure S19. Posterior distributions for V_{SV} (a,d,g,j,m,p), ξ (b,e,h,k,n,q) and V_{PH} (c,f,i,l,o,r) for six cross section points across North America (Figure S8) with respect to an isotropic reference model smoothed into Crust1.0 (gray line). The preferred median model for V_{SV} (red), ξ (blue) and V_{PH} (green) is shown as a solid, bold line. Confidence intervals (percentage of models) are shown as varying shades of red (V_{SV}), blue (ξ) and green (V_{PH}). Data misfit (X_D^2) is also reported.

LSQR Data Inversions

Figures S20–S23 detail inversion results for twelve craton locations (Figures S20–S21), five tectonically active locations (Figure S22) and six cross section points across North America (Figure S23) computed using the LSQR algorithm.

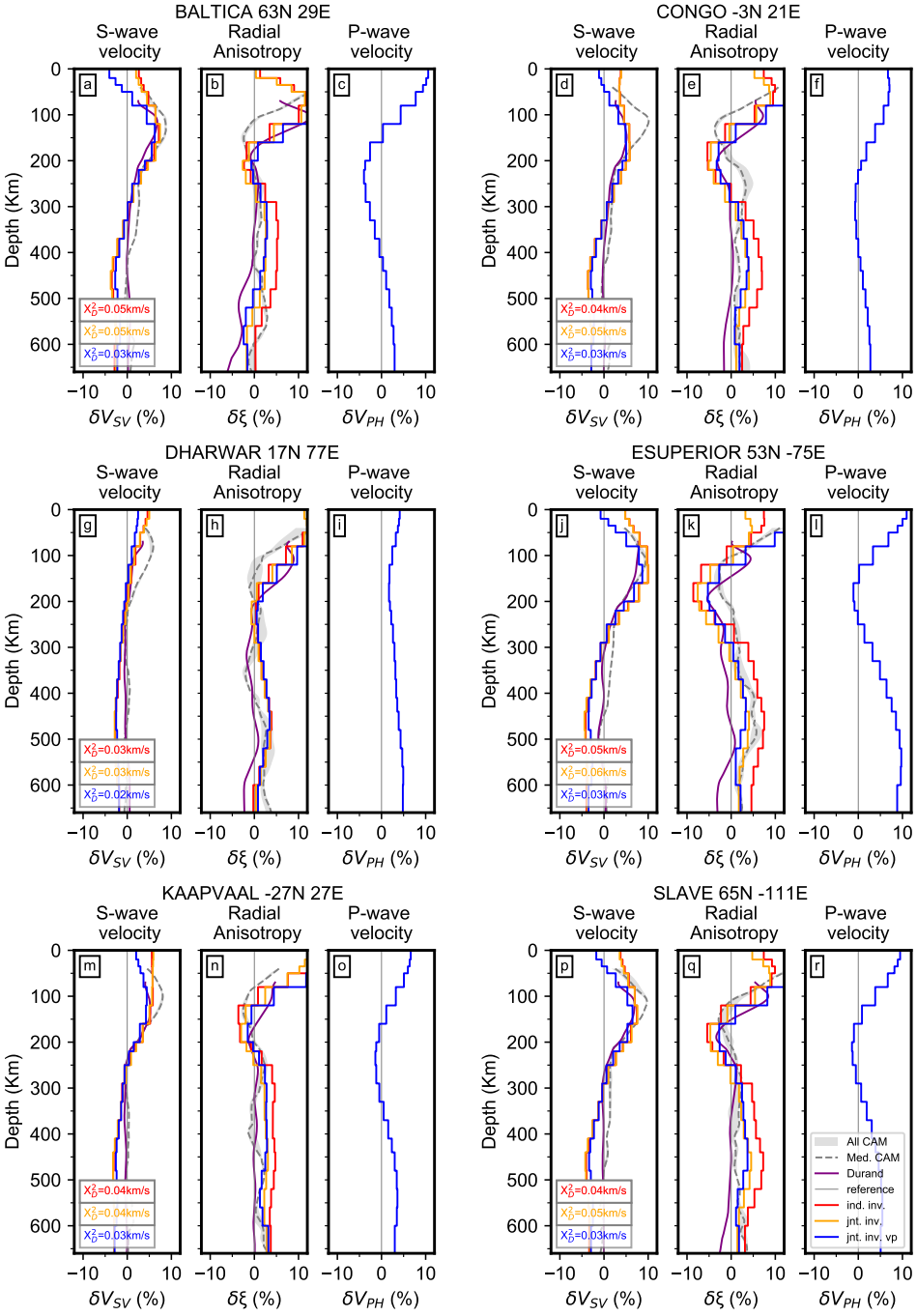

Figure S20. Data from six cratonic locations (Figure S6) inverted using variably parameterized LSQR algorithm after Tarantola and Valette (1982). V_{SV} (a,d,g,j,m,p), ξ (b,e,h,k,n,q) and V_{PH} (c,f,i,l,o,r) shown in percent deviation from isotropic reference model (gray line). Red curve: Independent inversion for V_{SV} and V_{SH}, Orange curve: Joint inversion for V_{SV} and V_{SH}, Blue curve: Joint inversion for V_{SV}, V_{SH} and V_{PH}. Chi squared data (X_D^2) fits shown. Gray shaded regions and dashed curve (med. mod) show distribution of V_{SV} and ξ profiles from CAM2016 model (Priestley et al., 2020) extracted at each location. Profiles from *Durand2023 - unpublished* are shown in purple.

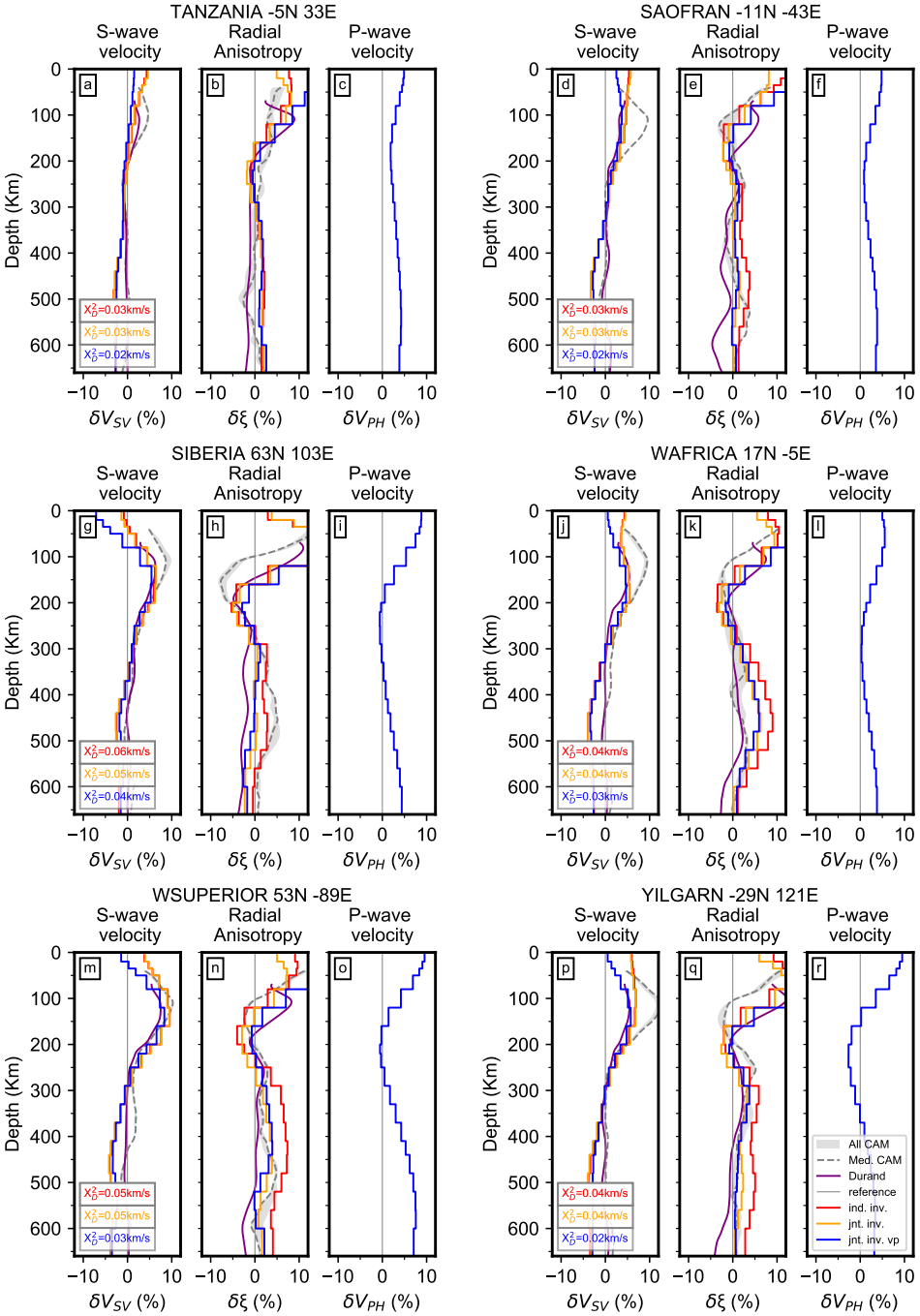

Figure S21. Data from six cratonic locations (Figure S6) inverted using variably parameterized LSQR algorithm after Tarantola and Valette (1982). V_{SV} (a,d,g,j,m,p), ξ (b,e,h,k,n,q) and V_{PH} (c,f,i,l,o,r) shown in percent deviation from isotropic reference model (gray line). Red curve: Independent inversion for V_{SV} and V_{SH}, Orange curve: Joint inversion for V_{SV} and V_{SH}, Blue curve: Joint inversion for V_{SV}, V_{SH} and V_{PH}. Chi squared data (X^2_D) fits shown. Gray shaded regions and dashed curve (med. mod) show distribution of V_{SV} and ξ profiles from CAM2016 model (Priestley et al., 2020) extracted at each location. Profiles from *Durand2023 - unpublished* are shown in purple.

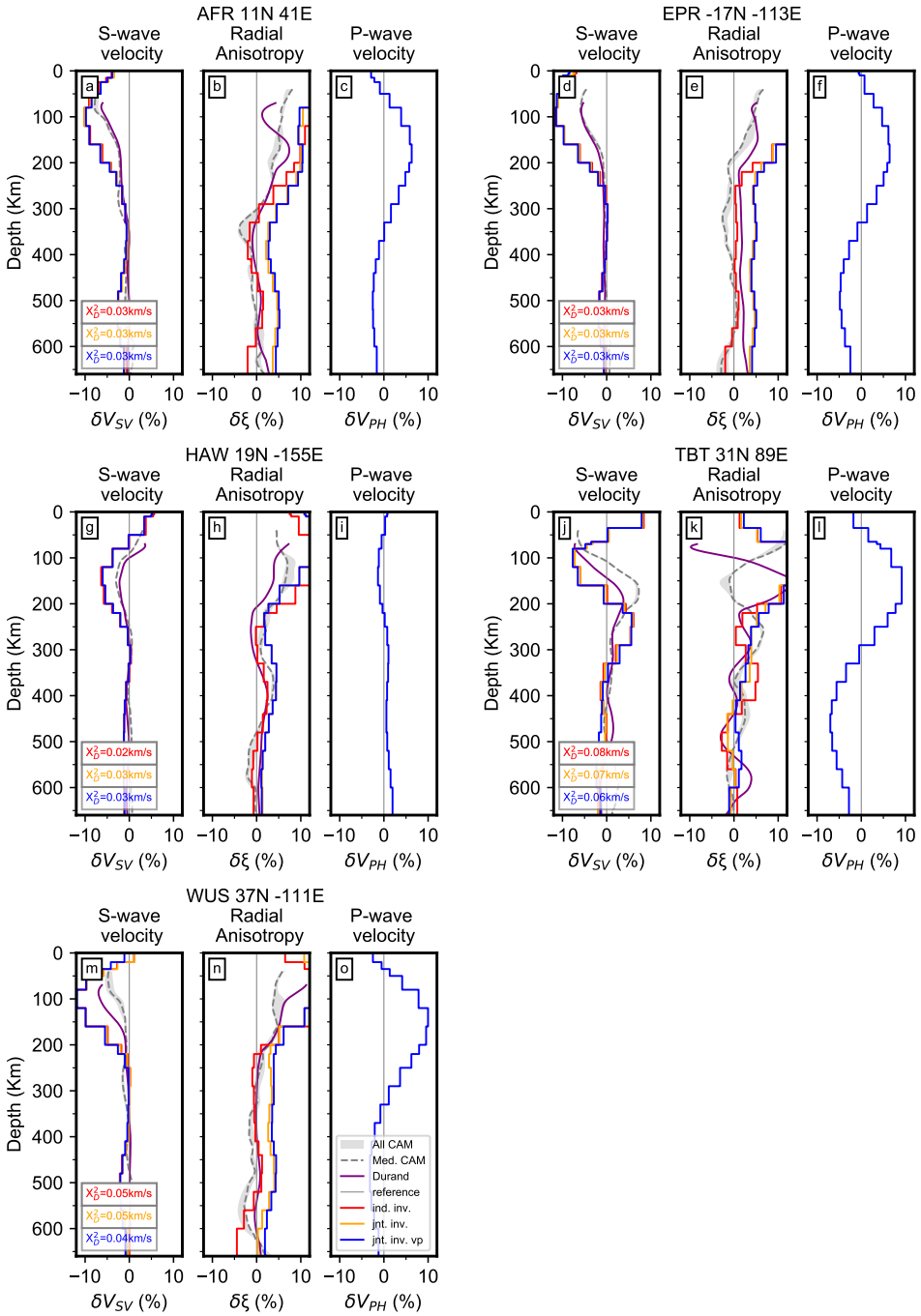

Figure S22. Data from five active tectonic locations (Figure S7) inverted using variably parameterized LSQR algorithm after Tarantola and Valette (1982). V_{SV} (a,d,g,j,m,p), ξ (b,e,h,k,n,q) and V_{PH} (c,f,i,l,o,r) shown in percent deviation from isotropic reference model (gray line). Red curve: Independent inversion for V_{SV} and V_{SH}, Orange curve: Joint inversion for V_{SV} and V_{SH}, Blue curve: Joint inversion for V_{SV}, V_{SH} and V_{PH}. Chi squared data (X_D^2) fits shown. Gray shaded regions and dashed curve (med. mod) show distribution of V_{SV} and ξ profiles from CAM2016 model (Priestley et al., 2020) extracted at each location. Profiles from *Durand2023 - unpublished* are shown in purple.

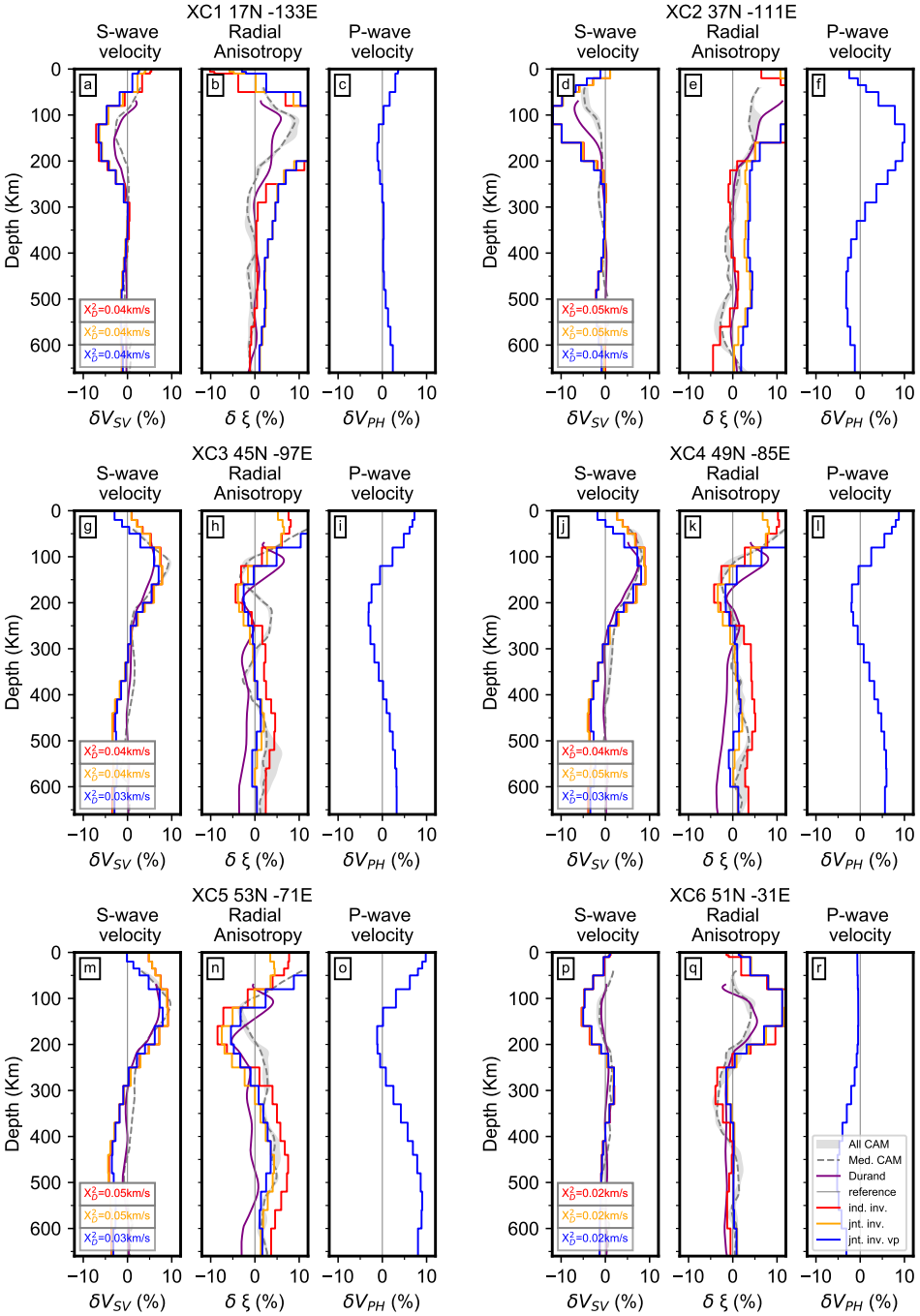

Figure S23. Data from six cross section points across North America (Figure S8) inverted using variably parameterized LSQR algorithm after Tarantola and Valette (1982). V_{SV} (a,d,g,j,m,p), ξ (b,e,h,k,n,q) and V_{PH} (c,f,i,l,o,r) shown in percent deviation from isotropic reference model (gray line). Red curve: Independent inversion for V_{SV} and V_{SH}, Orange curve: Joint inversion for V_{SV} and V_{SH}, Blue curve: Joint inversion for V_{SV}, V_{SH} and V_{PH}. Chi squared data (X_D^2) fits shown. Gray shaded regions and dashed curve (med. mod) show distribution of V_{SV} and ξ profiles from CAM2016 model (Priestley et al., 2020) extracted at each location. Profiles from *Durand2023 - unpublished* are shown in purple.

Synthetic Tests for Interpretations

To verify whether strong horizontal layering, or extrinsic anisotropy, can reproduce our real data inversions we conduct three synthetic tests with increasing strength of extrinsic anisotropy composed of 5 km thick layers and 0 to +10-40% V_{SV} velocity anomalies in each layer. Greater than 20% variation is required to induce apparent anisotropy in the median model within the posterior distributions. We consider that such extrinsic anisotropy is likely to be unrealistic.

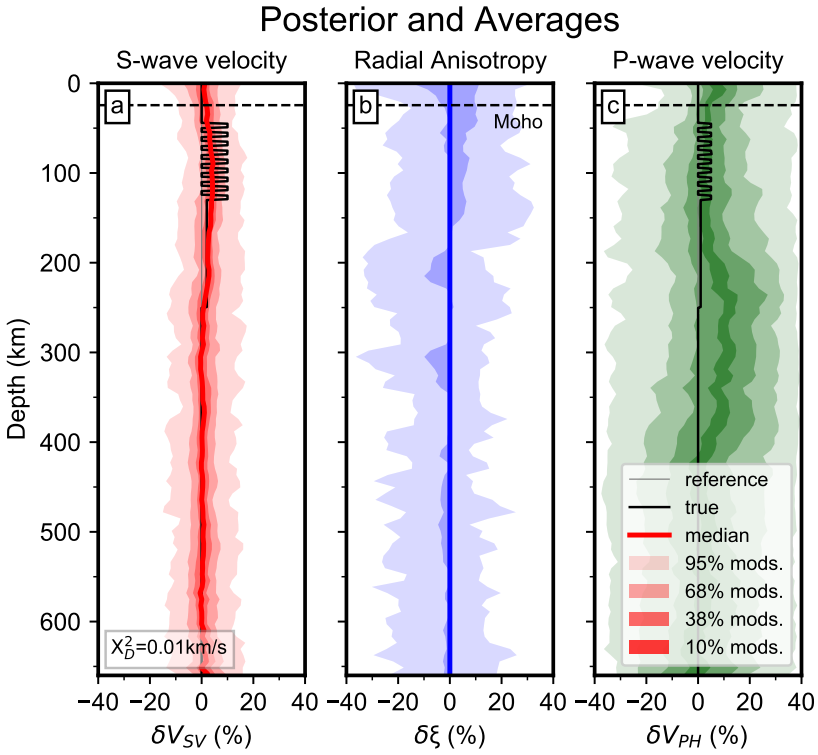

Figure S24. Posterior distributions for V_{SV} (a), ξ (b) and V_{PH} (c) for inversion of an extrinsically anisotropic synthetic model (thick black line, 10% variation) plotted with respect to an isotropic reference model (gray line). The preferred median model for V_{SV} (red), ξ (blue) and V_{PH} (green) is shown as a solid, bold line. Confidence intervals (percentage of models) are shown as varying shades of red (V_{SV}), blue (ξ) and green (V_{PH}). Data misfit (X_D^2) is also reported.

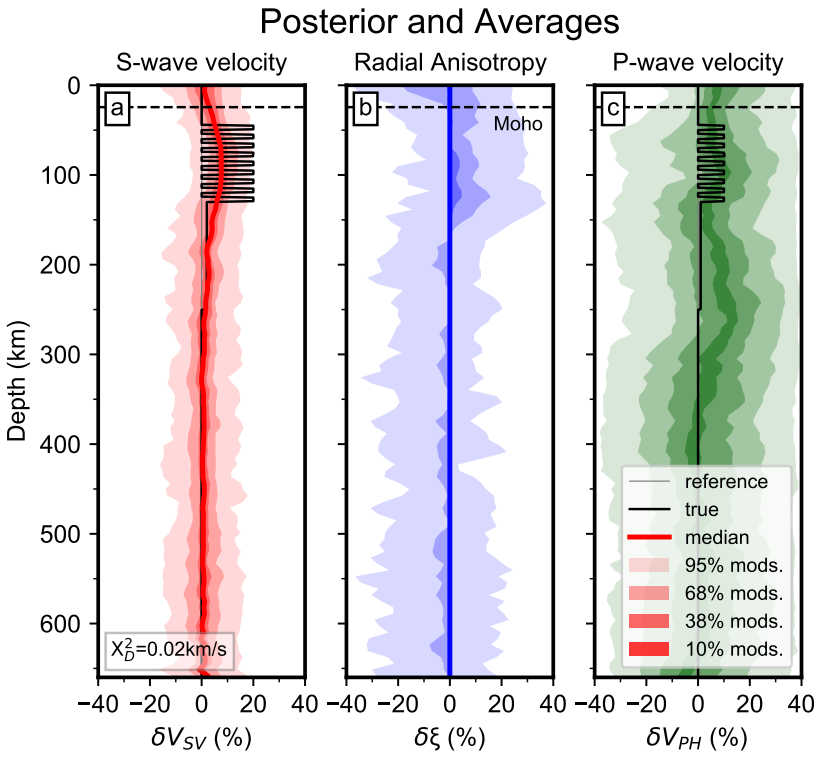

Figure S25. Posterior distributions for V_{SV} (a), ξ (b) and V_{PH} (c) for inversion of an extrinsically anisotropic synthetic model (thick black line, 20% variation) plotted with respect to an isotropic reference model (gray line). The preferred median model for V_{SV} (red), ξ (blue) and V_{PH} (green) is shown as a solid, bold line. Confidence intervals (percentage of models) are shown as varying shades of red (V_{SV}), blue (ξ) and green (V_{PH}). Data misfit (X_D^2) is also reported.

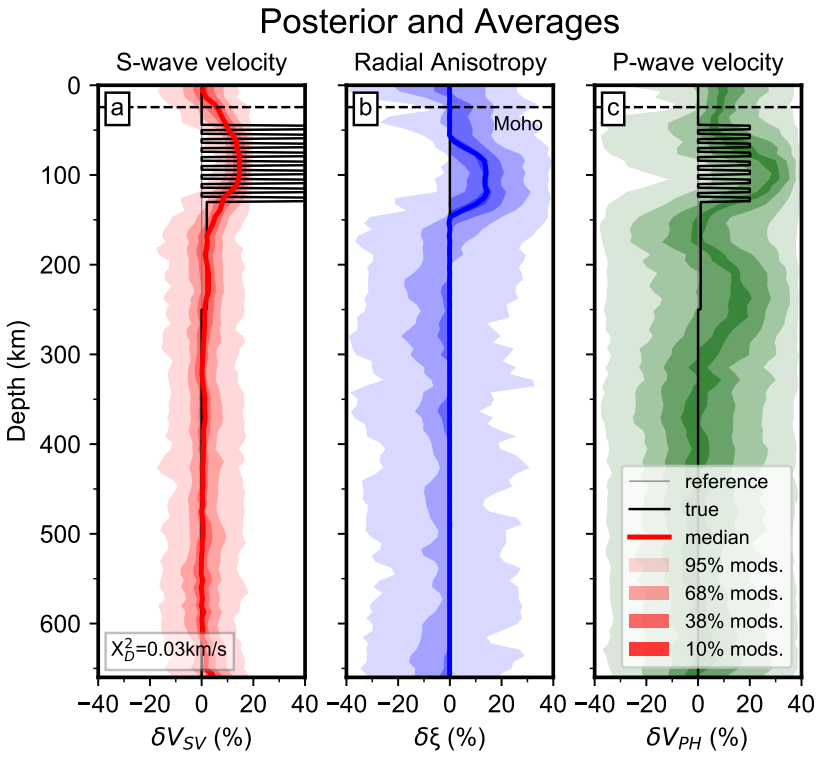

Figure S26. Posterior distributions for V_{SV} (a), ξ (b) and V_{PH} (c) for inversion of an extrinsically anisotropic synthetic model (thick black line, 40% variation) plotted with respect to an isotropic reference model (gray line). The preferred median model for V_{SV} (red), ξ (blue) and V_{PH} (green) is shown as a solid, bold line. Confidence intervals (percentage of models) are shown as varying shades of red (V_{SV}), blue (ξ) and green (V_{PH}). Data misfit (X_D^2) is also reported.

Figure S27 shows an alternate generalized synthetic model including strong horizontal layering (extrinsic anisotropy) in the low velocity zone which is indistinguishable from that presented in the main manuscript Figure 3.

In order to verify the robustness of our SRF forward modeling approach we include Figures S28–S30. Note that all velocity and anisotropy anomalies are plotted relative to the reference model. We track the depth difference between the known interface in the input synthetic model and peak produced in the SRF stacked trace (ε). We also indicate the depth range of peaks within individual SRFs that contribute to a specific peak within the SRF stack (δz).

Figure S28 shows that an SRF stack forward modeled from the reference model (i.e. zero anomaly input model) produces a positive peak within 2.3 km of the reference model Moho discontinuity, as expected (at 24.4 km depth in simplified PREM-like reference model). The slightly shallower depth of the peak in the SRF, compared to the input model, may be associated with interference from a positive phase arriving from the mid-crustal interface (at 15 km depth) in the reference model.

Figure S29 shows that when sufficiently separated in depth, a positive amplitude peak is found within 5.6 km depth of a 6% velocity increase at 130 km depth, as seen in Figure 3 of the main manuscript. The relatively muted amplitude of this phase likely results from a high depth range of peaks from individual SRFs contributing to the peak on the stacked trace ($\delta z = \pm 10.0$ km). An underlying 6% velocity decrease at 250 km depth also produces a negative amplitude arrival within 7.1 km depth.

Figure S30 shows that the negative amplitude arrival from the NVG (MLD or top of LVZ) within our proposed synthetic model (from Figure 3) lies within 1.3 km depth of the input anomaly depth (of 90 km). The relatively high amplitude of this phase likely results from a low depth range of peaks from individual SRFs contributing to the peak on the stacked trace ($\delta z = \pm 2.5$ km). The downward offset of the Moho phase by 6.7 km is likely due to interference with a positive arrival associated with the positive velocity jump at 45 km depth in the input model. The absolute velocity jump at the Moho is greater than that at 45 km depth in the input model, so is the dominant phase.

We suggest that some displacement/lack of apparent phases in the forward modeled SRF stack for the proposed model (in Figure 3) is mostly therefore due to interfer-

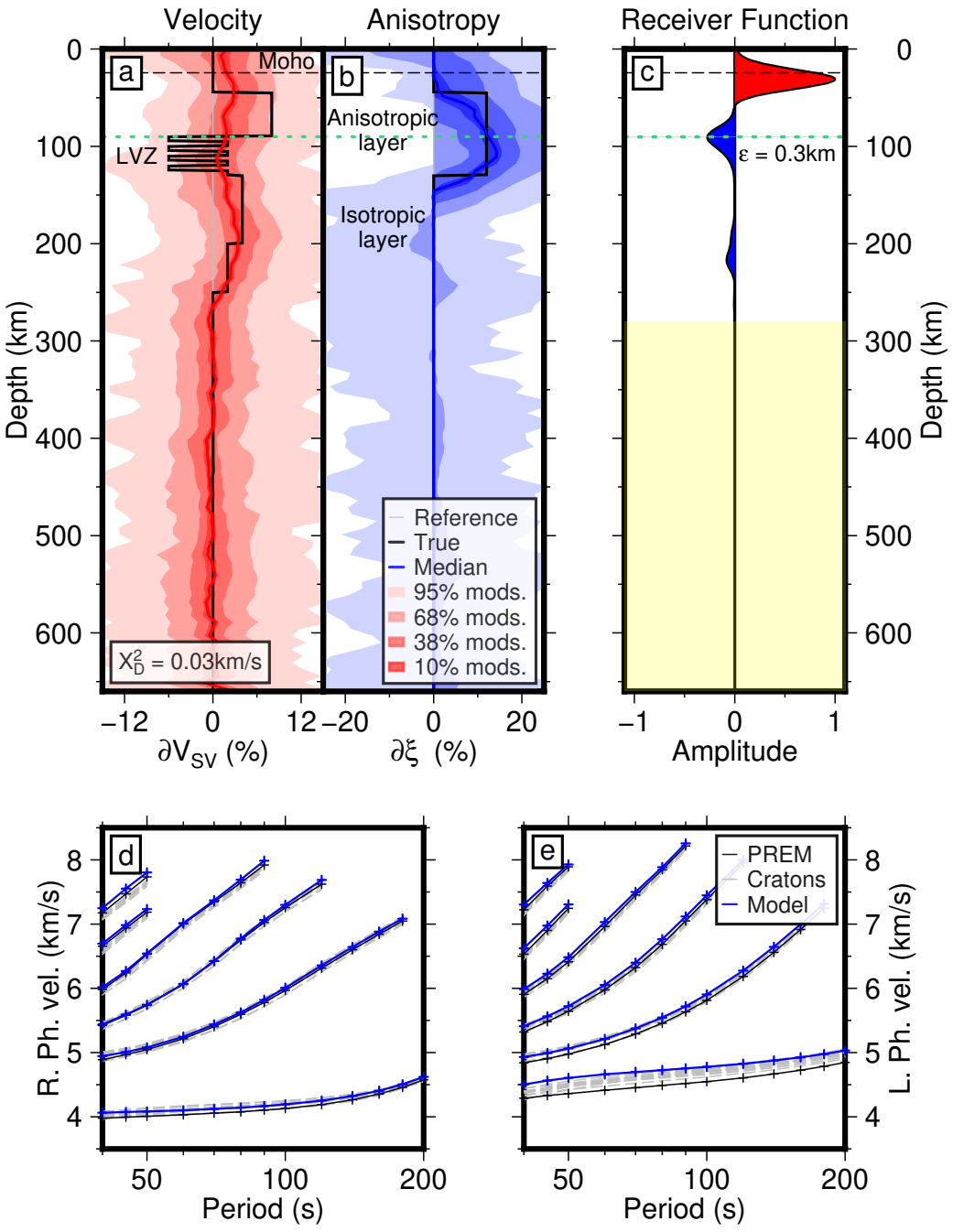

Figure S27. Posterior distributions for V_{SV} (a) and ξ (b) for an alternate generalized synthetic model (bold black line) with respect to the isotropic reference model (gray line). The preferred median model for V_{SV} (red) and ξ (blue) is shown as a solid, bold line. Confidence intervals (percentage of models) are shown as varying shades of red (V_{SV}) and blue (ξ). Data misfit (X_D^2) is also reported. Axisem simulation (Nissen-Meyer et al., 2014) through synthetic model used to generate S-to-p Receiver Function (RF) stack (c) constructed using RFs between 79–84° epicentral distance. Green horizontal dashed lines show depth difference (ε) between input discontinuity and maximum amplitude on the SRF. Yellow shaded region is below RF stacking depth. Rayleigh (d) and Love (e) fundamental and overtone (1–5) dispersion curves used in the inversions.

ing phases in the period range used here which are similar to those used in the literature for both synthetic and real data studies. We estimate that within our forward modeling, the depth of the observed NVG (70–130 km depth) may have a maximum error of up to ~5 km.

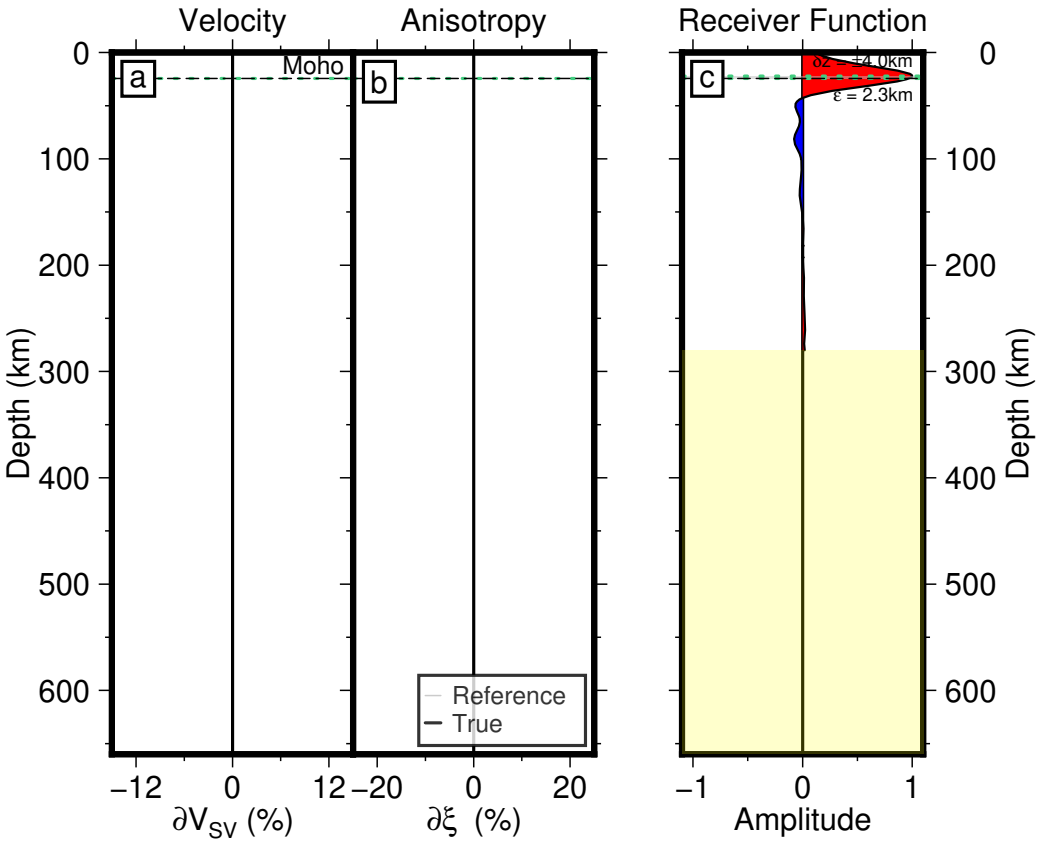

Figure S28. A zero anomaly input δV_{SV} (a) and $\delta\xi$ (b) synthetic model (bold black line) with respect to isotropic reference model (gray line) is used to forward model an S-to-p Receiver Function (SRF) stack (c) obtained from spectral element simulations (Axisem). Green horizontal dashed lines (and gray shaded area between) show depth difference (ε) between input discontinuity and maximum amplitude on the SRF. δz gives the range of depths for each peak within each individual RF trace contributing to the stack.

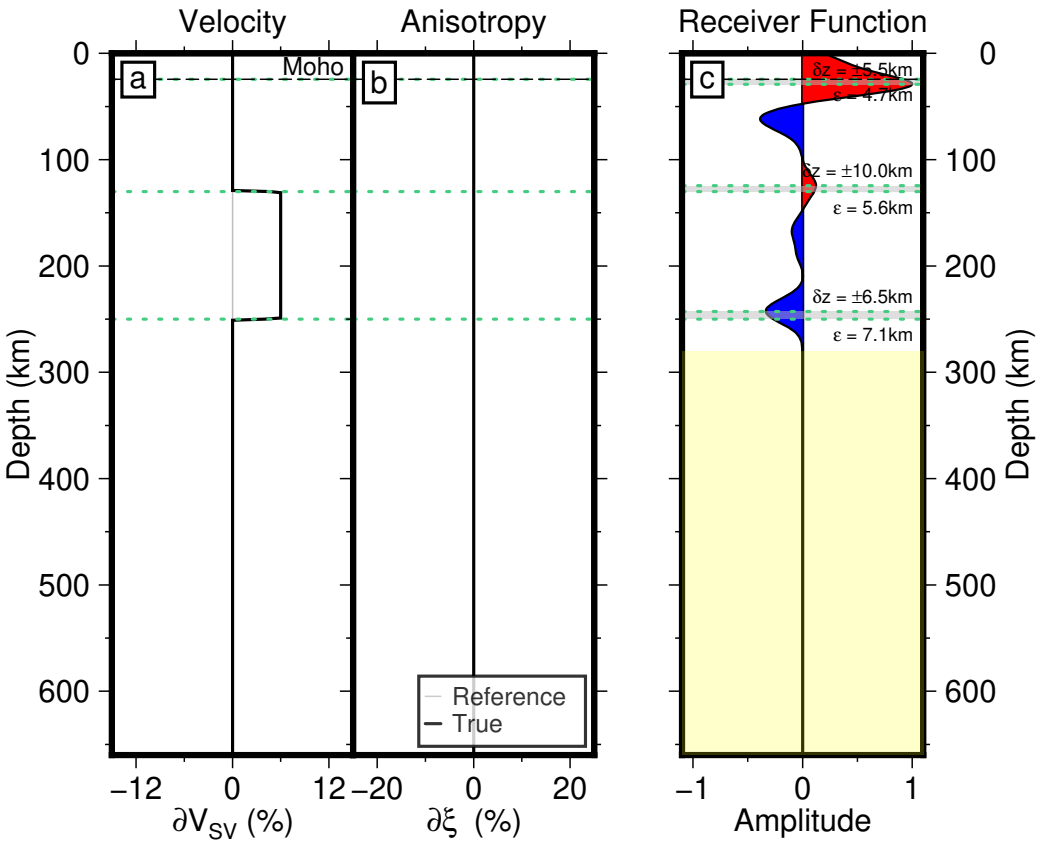

Figure S29. A positive δV_{SV} anomaly (a) and zero $\delta\xi$ anomaly (b) input synthetic model (bold black line) with respect to isotropic reference model (gray line) is used to forward model an S-to-p Receiver Function (SRF) stack (c) obtained from spectral element simulations (Axisem). Green horizontal dashed lines (and gray shaded area between) show depth difference (ε) between input discontinuity and maximum amplitude on the SRF. δz gives the range of depths for each peak within each individual RF trace contributing to the stack. The strong negative peak at 60 km depth results from a strong phase arrival prior to main S phase associated with the input model geometry, visible in 75–80° epicentral central distance range. This phase does not exist in the forward modeled wavefields for other input models.

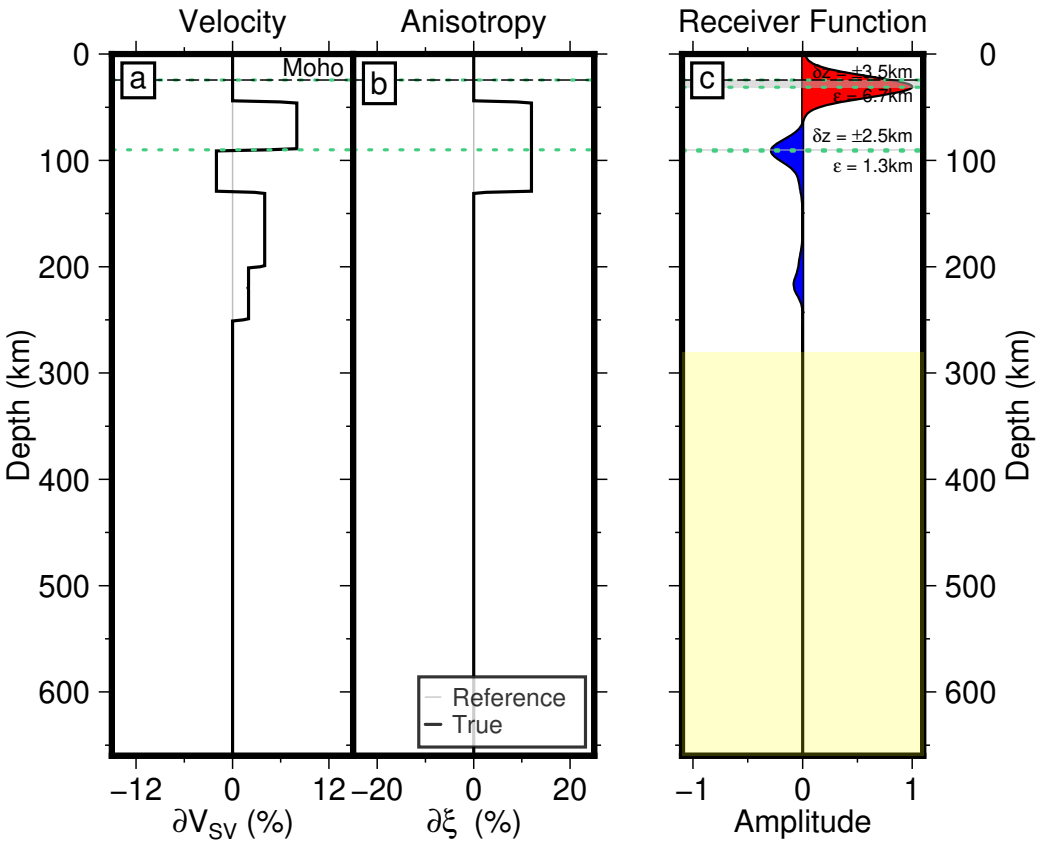

Figure S30. Proposed input synthetic δV_{SV} (a) and $\delta\xi$ (b) anomaly model from Figure 3 (bold black line) with respect to isotropic reference model (gray line) is used to forward model an S-to-p Receiver Function (SRF) stack (c) obtained from spectral element simulations (Axisem). Green horizontal dashed lines (and gray shaded area between) show depth difference (ε) between input discontinuity and maximum amplitude on the SRF. δz gives the range of depths for each peak within each individual RF trace contributing to the stack.

NVG Database

Improving on the database of Rader et al. (2015), we assemble a database of negative velocity gradient (NVG) depths using predominantly S-to-p receiver function results from the following works: Abt et al. (2010); Birkey et al. (2021); Bodin et al. (2014); Courtier and Revenaugh (2006); Dündar et al. (2011); Ford et al. (2010, 2016); Geissler et al. (2010); Heit et al. (2007); Heuer et al. (2007); Kawakatsu et al. (2009); Krueger et al. (2021); Kumar, Kind, et al. (2005); Kumar, Yuan, et al. (2005); Kumar et al. (2006); Kumar, Kind, et al. (2007); Kumar, Yuan, et al. (2007); Kumar et al. (2012, 2013); Li et al. (2004, 2007); Miller and Eaton (2010); Mohsen et al. (2006); Revenaugh and Sipkin (1994); Rychert et al. (2005, 2007); Rychert and Shearer (2009); Saul et al. (2000); Selway et al. (2015); Sodoudi, Kind, et al. (2006); Sodoudi, Yuan, et al. (2006); Sodoudi et al. (2009); Wirth and Long (2014); Wölbern et al. (2012); Yuan et al. (2006); J. Zhao et al. (2010); W. Zhao et al. (2011); Zheng and Romanowicz (2012). We distribute this compiled database alongside our manuscript "MLD_compilation_BOYCE_2023.xlsx" under the doi: 10.5281/zenodo.8167649 (Boyce, 2023).

Next, we merge this database with the recently published database of Fu et al. (2022) by selecting entries with a minimum horizontal and vertical separation distance of 50 km and 20 km respectively, to avoid duplication. We exclude results extracted visually from stacked profiles or broad areas that may lead to bias or inaccuracies. When computing spatial statistics we take mean values in 2° bins to avoid spatial sampling biases (e.g., Rader et al., 2015).

We note that depth uncertainties within our database are most strongly influenced by time-to-depth corrections applied to the data in each study. Comparison of our own synthetic data stacks, depth corrected using both PREM and the appropriate synthetic model, suggests that NVG depth uncertainties at mid-lithospheric depths may be on the order of ∼10 km, in line with scarcely published uncertainties (e.g., Ford et al., 2010; Birkey et al., 2021, see compiled database).

References

Abt, D. L., Fischer, K. M., French, S. W., Ford, H. A., Yuan, H., & Romanowicz, B. (2010). North American lithospheric discontinuity structure imaged by Ps and Sp receiver functions. *J. Geophys. Res.*, *115*. doi: 10.1029/2009JB006914

Auer, L., Boschi, L., Becker, T. W., Nissen-Meyer, T., & Giardini, D. (2014). Savani : A variable resolution whole-mantle model of anisotropic shear velocity variations based on multiple data sets. *J. Geophys. Res.*, *119*(4), 3006–3034. doi: 10.1002/2013jb010773

Birkey, A., Ford, H. A., Dabney, P., & Goldhagen, G. (2021). The Lithospheric Architecture of Australia From Seismic Receiver Functions. *J. Geophys. Res.*, *126*(4). doi: 10.1029/2020jb020999

Bodin, T., Yuan, H., & Romanowicz, B. (2014). Inversion of receiver functions without deconvolution—application to the Indian craton. *Geophys. J. Int.*, *196*(2), 1025–1033. doi: 10.1093/gji/ggt431

Boyce, A. (2023). *Craton Radial Anisotropy and Low Velocity Zones imaged with Bayesian and LSQR methods* [Dataset]. Zenodo. Retrieved from `https://doi.org/10.5281/zenodo.8167649` doi: 10.5281/zenodo.8167649

Chang, S. J., Ferreira, A. M. G., Ritsema, J., Van Heijst, H.-J., & Woodhouse, J. H. (2015). Joint inversion for global isotropic and radially anisotropic mantle structure including crustal thickness perturbations. *J. Geophys. Res.*, *120*(6), 4278–4300. doi: 10.1002/2014jb011824

Courtier, A. M., & Revenaugh, J. (2006). Earth's Deep Water Cycle. *Geophysical Monograph Series*, 181–193. doi: 10.1029/168gm14

Dündar, S., Kind, R., Yuan, X., Bulut, F., Sodoudi, F., Heit, B., ... Davila, J. M. (2011). Receiver function images of the base of the lithosphere in the Alboran Sea region. *Geophys. J. Int.*, *187*(2), 1019–1026. doi: 10.1111/j.1365-246x.2011.05216.x

Durand, S., Debayle, E., & Ricard, Y. (2015). Rayleigh wave phase velocity and error maps up to the fifth overtone [Dataset]. *Geophys. Res. Lett.*, *42*(9), 3266–3272. doi: 10.1002/2015gl063700

Dziewonski, A. M., & Anderson, D. L. (1981). Preliminary reference Earth model. *Phys. Earth Planet. Int.*, *25*(4), 297–356. doi: 10.1016/0031-9201(81)90046-7

Ford, H. A., Fischer, K. M., Abt, D. L., Rychert, C. A., & Elkins-Tanton, L. T. (2010). The lithosphere–asthenosphere boundary and cratonic lithospheric layering beneath Australia from Sp wave imaging. *Earth Planet. Sci. Lett.*, *300*(3-4), 299–310. doi: 10.1016/j.epsl.2010.10.007

Ford, H. A., Long, M. D., & Wirth, E. A. (2016). Midlithospheric discontinu-

ities and complex anisotropic layering in the mantle lithosphere beneath the Wyoming and Superior Provinces. *J. Geophys. Res.*, *121*(9), 6675–6697. doi: 10.1002/2016jb012978

French, S. W., & Romanowicz, B. (2014). Whole-mantle radially anisotropic shear velocity structure from spectral-element waveform tomography. *Geophys. J. Int.*, *199*(3), 1303–1327. doi: 10.1093/gji/ggu334

Fu, H., Li, Z., & Chen, L. (2022). Continental Mid-Lithosphere Discontinuity: A Water Collector During Craton Evolution. *Geophys. Res. Lett.*, *49*(23). doi: 10.1029/2022gl101569

Geissler, W. H., Sodoudi, F., & Kind, R. (2010). Thickness of the central and eastern European lithosphere as seen by S receiver functions. *Geophys. J. Int.*, *181*(2), 604–634. doi: 10.1111/j.1365-246x.2010.04548.x

Heit, B., Sodoudi, F., Yuan, X., Bianchi, M., & Kind, R. (2007). An S receiver function analysis of the lithospheric structure in South America. *Geophys. Res. Lett.*, *34*(14). doi: 10.1029/2007gl030317

Heuer, B., Kämpf, H., Kind, R., & Geissler, W. H. (2007). Seismic evidence for whole lithosphere separation between Saxothuringian and Moldanubian tectonic units in central Europe. *Geophys. Res. Lett.*, *34*(9). doi: 10.1029/2006gl029188

Ho, T., Priestley, K., & Debayle, E. (2016). A global horizontal shear velocity model of the upper mantle from multimode Love wave measurements [Dataset]. *Geophys. J. Int.*, *207*(1), 542–561. doi: 10.1093/gji/ggw292

Kawakatsu, H., Kumar, P., Takei, Y., Shinohara, M., Kanazawa, T., Araki, E., & Suyehiro, K. (2009). Seismic Evidence for Sharp Lithosphere-Asthenosphere Boundaries of Oceanic Plates. *Science*, *324*(5926), 499–502. doi: 10.1126/science.1169499

Krueger, H. E., Gama, I., & Fischer, K. M. (2021). Global Patterns in Cratonic Mid-Lithospheric Discontinuities from Sp Receiver Functions. *Geochem. Geophys. Geosyst.*. doi: 10.1029/2021gc009819

Kumar, P., Kind, R., Hanka, W., Wylegalla, K., Reigber, C., Yuan, X., ... Wolf, D. (2005). The lithosphere–asthenosphere boundary in the North-West Atlantic region. *Earth Planet. Sci. Lett.*, *236*(1-2), 249–257. doi: 10.1016/j.epsl.2005.05.029

Kumar, P., Kind, R., Priestley, K., & Dahl-Jensen, T. (2007). Crustal structure of Iceland and Greenland from receiver function studies. *J. Geophys. Res.*, *112*(B3). doi: 10.1029/2005jb003991

Kumar, P., Kumar, M. R., Srijayanthi, G., Arora, K., Srinagesh, D., Chadha, R. K., & Sen, M. K. (2013). Imaging the lithosphere-asthenosphere boundary of the Indian plate using converted wave techniques. *J. Geophys. Res.*, *118*(10), 5307–5319. doi: 10.1002/jgrb.50366

Kumar, P., Yuan, X., Kind, R., & Kosarev, G. (2005). The lithosphere-asthenosphere boundary in the Tien Shan-Karakoram region from S receiver functions: Evidence for continental subduction. *Geophys. Res. Lett.*, *32*(7). doi: 10.1029/2004gl022291

Kumar, P., Yuan, X., Kind, R., & Mechie, J. (2012). The lithosphere-asthenosphere boundary observed with USArray receiver functions. *Solid Earth*, *3*(1), 149–159. doi: 10.5194/se-3-149-2012

Kumar, P., Yuan, X., Kind, R., & Ni, J. (2006). Imaging the colliding Indian and Asian lithospheric plates beneath Tibet. *J. Geophys. Res.*, *111*(B6). doi: 10 .1029/2005jb003930

Kumar, P., Yuan, X., Kumar, M. R., Kind, R., Li, X., & Chadha, R. K. (2007). The rapid drift of the Indian tectonic plate. *Nature*, *449*(7164), 894–897. doi: 10 .1038/nature06214

Kustowski, B., Ekström, G., & Dziewoński, A. M. (2008). Anisotropic shear-wave velocity structure of the Earth's mantle: A global model. *J. Geophys. Res.*, *113*(B6). doi: 10.1029/2007jb005169

Laske, G., Masters, G., Ma, Z., & Pasyanos, M. E. (2013). Update on CRUST1.0 - A 1-degree Global Model of Earth's Crust. In *Geophys. res. abstracts, 15, abstract egu2013-2658* (p. EGU2013-2658).

Lei, W., Ruan, Y., Bozdağ, E., Peter, D., Lefebvre, M., Komatitsch, D., ... Pugmire, D. (2020). Global adjoint tomography—model GLAD-M25. *Geophys. J. Int.*, *223*(1), 1–21. doi: 10.1093/gji/ggaa253

Lekić, V., & Romanowicz, B. (2011). Inferring upper-mantle structure by full waveform tomography with the spectral element method. *Geophys. J. Int.*, *185*(2), 799–831. doi: 10.1111/j.1365-246X.2011.04969.x

Li, X., Kind, R., Yuan, X., Wölbern, I., & Hanka, W. (2004). Rejuvenation of the

lithosphere by the Hawaiian plume. *Nature*, *427*(6977), 827–829. doi: 10.1038/nature02349

Li, X., Yuan, X., & Kind, R. (2007). The lithosphere–asthenosphere boundary beneath the western United States. *Geophys. J. Int.*, *170*(2), 700–710. doi: 10.1111/j.1365-246x.2007.03428.x

Masters, G., Woodhouse, J. H., & Freeman, G. (2011). *Mineos v1.0.2* [Software]. Computational Infrastructure for Geodynamics. Retrieved from `https://geodynamics.org/cig/software/mineos/` (Published under the GPL2 license)

Megnin, C., & Romanowicz, B. (2000). The three-dimensional shear velocity structure of the mantle from the inversion of body, surface and higher-mode waveforms. *Geophys. J. Int.*, *143*(3), 709–728. doi: 10.1046/j.1365-246X.2000.00298.x

Miller, M. S., & Eaton, D. W. (2010). Formation of cratonic mantle keels by arc accretion: Evidence from S receiver functions. *Geophys. Res. Lett.*, *37*(18). doi: 10.1029/2010GL044366

Mohsen, A., Kind, R., Sobolev, S. V., Weber, M., & the DESERT Group. (2006). Thickness of the lithosphere east of the Dead Sea Transform. *Geophys. J. Int.*, *167*(2), 845–852. doi: 10.1111/j.1365-246x.2006.03185.x

Montagner, J. P., & Anderson, D. L. (1989). Petrological constraints on seismic anisotropy. *Phys. Earth Planet. Int.*, *54*(1-2), 82–105. doi: 10.1016/0031-9201(89)90189-1

Moulik, P., & Ekström, G. (2014). An anisotropic shear velocity model of the Earth's mantle using normal modes, body waves, surface waves and long-period waveforms. *Geophys. J. Int.*, *199*(3), 1713–1738. doi: 10.1093/gji/ggu356

Nissen-Meyer, T., van Driel, M., Stähler, S. C., Hosseini, K., Hempel, S., Auer, L., ... Fournier, A. (2014). AxiSEM: broadband 3-D seismic wavefields in axisymmetric media. *Solid Earth*, *5*(1), 425–445. doi: 10.5194/se-5-425-2014

Panning, M. P., Lekić, V., & Romanowicz, B. (2010). Importance of crustal corrections in the development of a new global model of radial anisotropy. *J. Geophys. Res.*, *115*(B12). doi: 10.1029/2010jb007520

Priestley, K., Ho, T., & McKenzie, D. (2020). The formation of continental roots.

Geology, *49*(2), 190-194. doi: 10.1130/G47696.1

Rader, E., Emry, E., Schmerr, N., Frost, D., Cheng, C., Menard, J., ... Geist, D. (2015). Characterization and Petrological Constraints of the Midlithospheric Discontinuity. *Geochem. Geophys. Geosyst.*, *16*(10), 3484–3504. doi: 10.1002/2015gc005943

Revenaugh, J., & Sipkin, S. A. (1994). Mantle discontinuity structure beneath China. *J. Geophys. Res.*, *99*(B11), 21911–21927. doi: 10.1029/94jb01850

Rychert, C. A., Fischer, K. M., & Rondenay, S. (2005). A sharp lithosphere–asthenosphere boundary imaged beneath eastern north america. *Nature*, *436*(7050), 542-545. doi: 10.1038/nature03904

Rychert, C. A., Rondenay, S., & Fischer, K. M. (2007). P-to-S and S-to-P imaging of a sharp lithosphere-asthenosphere boundary beneath eastern North America. *J. Geophys. Res.*, *112*(B8). doi: 10.1029/2006jb004619

Rychert, C. A., & Shearer, P. M. (2009). A Global View of the Lithosphere-Asthenosphere Boundary. *Science*, *324*(5926), 495–498. doi: 10.1126/science.1169754

Saul, J., Kumar, M. R., & Sarkar, D. (2000). Lithospheric and upper mantle structure of the Indian Shield, from teleseismic receiver functions. *Geophys. Res. Lett.*, *27*(16), 2357–2360. doi: 10.1029/1999gl011128

Selway, K., Ford, H., & Kelemen, P. (2015). The seismic mid-lithosphere discontinuity. *Earth Planet. Sci. Lett.*, *414*, 45–57. doi: 10.1016/j.epsl.2014.12.029

Simmons, N. A., Myers, S. C., Morency, C., Chiang, A., & Knapp, D. R. (2021). SPiRaL: a multiresolution global tomography model of seismic wave speeds and radial anisotropy variations in the crust and mantle. *Geophys. J. Int.*, *227*(2), 1366–1391. doi: 10.1093/gji/ggab277

Sodoudi, F., Kind, R., Hatzfeld, D., Priestley, K., Hanka, W., Wylegalla, K., ... Bohnhoff, M. (2006). Lithospheric structure of the Aegean obtained from P and S receiver functions. *J. Geophys. Res.*, *111*(B12). doi: 10.1029/2005jb003932

Sodoudi, F., Yuan, X., Kind, R., Heit, B., & Sadidkhouy, A. (2009). Evidence for a missing crustal root and a thin lithosphere beneath the Central Alborz by receiver function studies. *Geophys. J. Int.*, *177*(2), 733–742. doi: 10.1111/j.1365-246x.2009.04115.x

Sodoudi, F., Yuan, X., Liu, Q., Kind, R., & Chen, J. (2006). Lithospheric thickness beneath the Dabie Shan, central eastern China from S receiver functions. *Geophys. J. Int.*, *166*(3), 1363–1367. doi: 10.1111/j.1365-246x.2006.03080.x

Tarantola, A., & Valette, B. (1982). Generalized nonlinear inverse problems solved using the least squares criterion. *Reviews of Geophysics*, *20*(2), 219–232. doi: 10.1029/rg020i002p00219

Tesoniero, A., Auer, L., Boschi, L., & Cammarano, F. (2015). Hydration of marginal basins and compositional variations within the continental lithospheric mantle inferred from a new global model of shear and compressional velocity. *J. Geophys. Res.*, *120*(11), 7789–7813. doi: 10.1002/2015jb012026

Thrastarson, S., van Herwaarden, D.-P., Krischer, L., Boehm, C., van Driel, M., Afanasiev, M., & Fichtner, A. (2022). Data-adaptive global full-waveform inversion. *Geophys. J. Int.*, *230*(2), 1374–1393. doi: 10.1093/gji/ggac122

Wirth, E. A., & Long, M. D. (2014). A contrast in anisotropy across mid-lithospheric discontinuities beneath the central United States—A relic of craton formation. *Geology*, *42*(10), 851–854. doi: 10.1130/g35804.1

Wölbern, I., Rümpker, G., Link, K., & Sodoudi, F. (2012). Melt infiltration of the lower lithosphere beneath the Tanzania craton and the Albertine rift inferred from S receiver functions. *Geochem. Geophys. Geosyst.*, *13*(8). doi: 10.1029/2012gc004167

Yuan, X., Kind, R., Li, X., & Wang, R. (2006). The S receiver functions: synthetics and data example. *Geophys. J. Int.*, *165*(2), 555–564. doi: 10.1111/j.1365-246X.2006.02885.x

Zhao, J., Yuan, X., Liu, H., Kumar, P., Pei, S., Kind, R., ... Wang, W. (2010). The boundary between the Indian and Asian tectonic plates below Tibet. *Proc. Nat. Acad. Sci.*, *107*(25), 11229–11233. doi: 10.1073/pnas.1001921107

Zhao, W., Kumar, P., Mechie, J., Kind, R., Meissner, R., Wu, Z., ... Tilmann, F. (2011). Tibetan plate overriding the Asian plate in central and northern Tibet. *Nat. Geosci.*, *4*(12), 870–873. doi: 10.1038/ngeo1309

Zheng, Z., & Romanowicz, B. (2012). Do double 'SS precursors' mean double discontinuities? *Geophys. J. Int.*, *191*(3), 1361–1373. doi: 10.1111/j.1365-246x.2012.05683.x